

Aerothermodynamic Design Problems of Non-Winged Re-Entry Vehicles

The transport of payload into space, either suborbital, orbital or superorbital and its return to the Earth's surface, is known to require the development and construction of suitable vehicles which are able to withstand the very severe thermal and mechanical (pressure and shear stress) loads encountered during such a mission. In the early days of space exploration, the designers had the feeling that the vehicle shapes should be as simple and compact as possible. So, capsules and probes as the most important types of non-winged re-entry vehicles (RV-NW) were born.

In this chapter we deal with a few major aerothermodynamic design problems of RV-NW's. Aerothermodynamic phenomena, high Mach number and total enthalpy effects as well as particular trends in aerothermodynamics of RV-NW's are mostly similar to those of RV-W's, Sections 3.1 and 3.2. However, we consider also vehicles for re-entry from higher altitudes than treated in Chapter 3, and also vehicles operating in extraterrestrial atmospheres.

The lunar return of APOLLO takes place with a velocity much higher than those typical of RV-W's. Therefore we find in this case much more severe thermochemical phenomena. Also the flight in extraterrestrial atmosphere leads to further, specific thermo-chemical description problems. We abstain from giving an overview of the special aerothermodynamic issues of such vehicles.

First, a general overview of the topics treated is given, strategies for atmospheric entry and orbital transfers are sketched, and configurational aspects are discussed. Because RV-NW's as a rule have no aerodynamic stabilization, trim and control surfaces, we concentrate our considerations in two of the five main sections on issues of static and dynamic stability. A general treatment of static stability also of these vehicles is given in Chapter 7. The last section is dedicated to a discussion of thermal loads.

5.1 Introduction and Entry Strategies

The class of non-winged re-entry vehicles considered here comprises ballistic entry probes (Sub-Class 1), traditional capsules like APOLLO and SOYUZ (Sub-Class 2) as well as blunted cones and biconics (bicones and bent bicones) (Sub-Class 3). While, normally, the capsules do not have aerodynamic control surfaces, the sub-class of cones may have some, in particular body flaps for

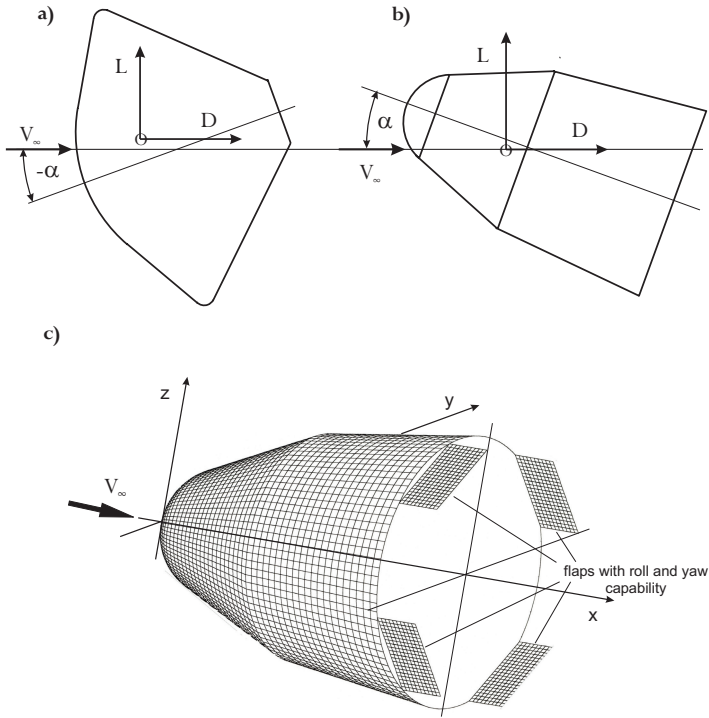


Fig. 5.1. Angle of attack for entry probe or capsule, a), and bicone, b), required for positive lift L . Sketch, illustrating the role of multi-functional control surfaces on bicones for pitch, yaw and roll, c).

longitudinal trim and, in case of multi-functional control surfaces with inclinations with respect to the lateral axis, also for roll control and lateral stability, Fig. 5.1 c).

For the capsule sub-class, the lift-to-drag ratio during atmospheric re-entry is mostly in the range of $0.3 \lesssim L/D \lesssim 0.4$. It should be mentioned here that, in order to avoid confusion, that for capsules, a positive lift will only be obtained for negative angles of attack (if classical aerodynamic definitions are used, Fig. 7.3), because the aerodynamic lift force is caused predominantly by the front part (heat shield) of the vehicle, Fig. 5.1 a), whereas in the case of a biconic, the lift force is brought about by the whole body, Fig. 5.1 b). The explanation of this behavior is given in Section 5.3. The aerodynamic efficiency of the blunted cone sub-class is somewhat higher and lies between $0.7 \lesssim L/D \lesssim 1.4$. In that case the contribution to the aerodynamic forces and moments is distributed over the whole body.

It is the intention of this chapter to provide the reader with detailed information about:

- the shape of some typical non-winged vehicles of the above mentioned three sub-classes,
- the requirements on their aerodynamic performance due to mission definition,
- some aspects of their aerodynamic data bases,
- static and dynamic stability,
- the role of the center-of-gravity regarding flyability and controllability,
- the influence of some geometrical shape variations on the aerodynamic coefficients,
- aerodynamic trim including parasite trim states,
- the influence of high temperature real gas effects on aerodynamic forces and moments as well as on aerodynamic trim,
- thermal loads.

To understand what kind of aerodynamic performance space vehicles must have and which thermal loads the configurations have to withstand, some terms describing the various strategies for atmospheric entry and transfer between orbits are now explained.

5.1.1 Aerobraking

Direct entry of probes and capsules into the atmosphere of any planet (Earth, Mars, Venus, Titan, etc.), where the entry velocity is strongly reduced to a low descent speed, is called aerobraking entry. In principle, it should always be possible to conduct an aerobraking entry if the following requirements can be satisfied (see also Chapter 2):

- resistance against thermal loads,
- minimization of vehicle mass \Rightarrow thermal protection system weight,
- restricted g -loads (n_t, n_n) \Rightarrow deceleration limit depending on payload,
- tolerable landing distortion (deviation from nominal landing position, recovery on ground or in water),
- minimum influence of atmospheric uncertainties¹ due to not well explored planets.

In reality, the entry strategy of a RV-NW has to be adjusted to the specific mission (entry velocity, entry angle, density of atmosphere, endurable g -loads, etc.) which results in the decision to use either a ballistic vehicle, or a low or a moderate L/D lifting vehicle. Additionally, it may be necessary to decrease the orbital velocity by a retro-rocket system or by an aerocapturing maneuver, e.g., in case of large entry velocity. The entry corridor is bounded by a certain low entry angle (shallow entry) beyond which the vehicle leaves the atmosphere again, and by a certain high entry angle (steep entry), above which the g -loads reach too high values or the aerothermal loads can not be mastered.

¹ This holds even for the Earth atmosphere, Chapter 2. For properties of the Earth atmosphere, see Appendix B.

Further, aerobraking is employed in order to support the initial propulsion boost during orbital transfer. Ballistic vehicles having no lift usually need a lot of passes through the atmosphere (e.g., for elliptic orbits in the periapsis regime of interplanetary missions) in order to reduce the speed for the target orbit, since the reduction per pass is low due to the limited energy reduction by aerodynamic drag in rarefied gas regimes [1].

5.1.2 Aerocapturing

The main problem for orbital transfer, planetary (Mars, Venus, Moon, etc.), and Earth return missions with high entry velocities is to properly diminish the energy of the vehicle, that is to reduce the velocity relative to the surface of the planet to be approached. Since the 1960s, studies were undertaken to develop the physical and technological basis for reducing velocities by aeroassisted orbital maneuvers [2]. A typical example of such a maneuver is as follows.

For an orbital transfer say, from geostationary (GEO) to low Earth orbit (LEO), the vehicle dips into the atmosphere, conducts an approximately constant drag flight controlled by the lifting capability until the velocity increment (Δv_∞) for a stable motion in the target orbit is reached, and skips back out of the atmosphere into just this target orbit. This process is called an aerocapturing mission.

In principle the flight control of the maneuver (lift control) can be carried out either by banking operations (see Chapter 2) or by angle of attack variations. Since the technology for lift control by pitch movement is rather complex and expensive in terms of system construction, in reality only bank-angle control systems are considered. The process described above is the same for a planetary mission (e.g. in the joint CNES–NASA Programme for Mars Sample Return [3]), where again the velocity decrement is achieved by a single sufficiently deep atmospheric pass to transfer the vehicle from its hyperbolic trajectory to the target orbit about the planet.

During the 1970s and the early 1980s, researchers had the opinion that aerocapturing maneuvers require vehicles with lift-to-drag values larger than unity, which can only be provided by slender or bent bicones. Further investigations have shown that the aerocapturing capability can also be achieved with vehicles having a $L/D \approx 0.3$ [1, 4], but the ballistic factor has to be low. In order to broaden the physical basis for this space-mission concept, a research programme was initiated in the U.S. named the Aeroassist Flight Experiment (AFE) [5].

5.1.3 Ballistic Flight—Ballistic Factor

Ballistic flight is flight without lift, i.e., $L = 0$. In the flight mechanical equations for space applications the factor

$$\beta_m = \frac{m}{A_{ref} C_D}, \quad (5.1)$$

called the ballistic factor or parameter, Sub-Section 2.1.1, with m being the mass, A_{ref} the reference area, and C_D the aerodynamic drag coefficient, plays a particular role [6, 7]. This quantity is a measure for the manner how probes perform a ballistic entry in any atmosphere with a specified landing distortion. Generally, the system concept manager of a space mission has to decide, considering budget, costs, mission and/or vehicle reliability, tolerable landing distortion and so on, which kind of atmospheric entry the capsule or probe should conduct: either ballistic or lifting.

Ballistic probes have the advantage that they do not require guidance and control precautions. Therefore these concepts are less costly than lifting ones but they need low ballistic factors for direct entry. Low ballistic factor means large reference area, high drag coefficient and low mass. Normally, for all known missions, an appropriate mass reduction is critical. The magnitude of drag is limited by the semi-apertural cone angle $\phi = \pi/2 - \Theta_1$, Figs. 5.3 and 5.4, which can cause static stability problems since the center-of-pressure is moved forward. A good compromise is a cone angle of $50^\circ \lesssim \phi \lesssim 70^\circ$ (HUYGENS and BEAGLE2: $\phi = 60^\circ$, OREX: $\phi = 50^\circ$).

A proper means for reducing the ballistic factor is to increase the frontal area A_{ref} . But one should have in mind that this could increase the thermal heat-shield mass. On the other hand, low ballistic factors provide low thermal loads. Finally, the nose radius R_1 , Fig. 5.3, does not affect very much the drag, but a large nose radius can contribute to a reduction of the mass of the thermal protection system (TPS) due to a decrease in the magnitude of the surface [1, 7]. An upper limit for the ballistic factor of ballistic vehicles seems to be $\beta_m \approx 60 \text{ kg/m}^2$. Lifting capsules, such as the ARD, APOLLO and VIKING can have much larger values since their entry flight can be guided and controlled by an onboard stability and control system, Table 5.1. Figure 5.2 shows a comparison of flight trajectories for a ballistic re-entry of the OREX and a low L/D re-entry ARD.

5.2 General Configurational Aspects

5.2.1 Ballistic Probes

In the past, there were some scientific space exploratory missions to other planets or moons of planets of the Solar system using ballistic probes. In the early days of space exploration, the probes PIONEER (1978) and MERCURY orbiter (1959–1963) were flown to the planet Venus, VIKING (1975–1982) (with some lifting capability) traveled to Mars and GALILEO (1989–1995) went to the planet Jupiter.

Since the Saturn moon Titan has an atmosphere, from which some scientists expect that extra-terrestrial life will develop in the future, the European HUYGENS probe was designed in the 1990s in order to explore the atmosphere and

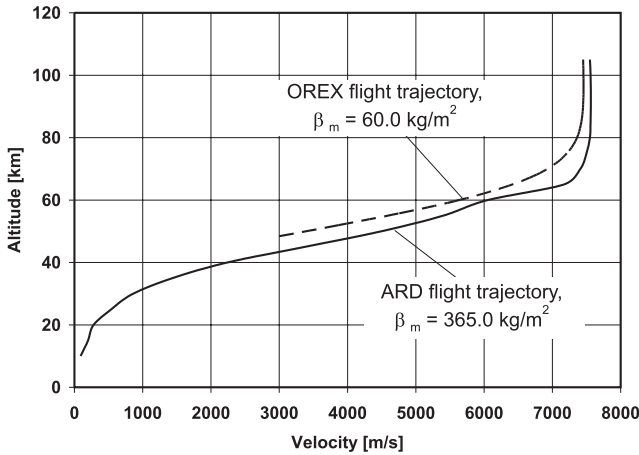


Fig. 5.2. Flight trajectories of OREX [8] and ARD [9].

ground conditions. It was launched in 1997 as a passenger on-board the American Mariner-Mark II CASSINI orbiter. After a flight of roughly seven years HUYGENS conducted a very successful entry into the Titan atmosphere in January 2005.

To ensure a stable ballistic flight and to master the thermal loads during entry in a not well-known atmosphere was the aerothermodynamic challenge of this mission. The composition of Titan’s atmosphere consists approximately of 87 per cent N_2 , 10 per cent Ar and 3 per cent CH_4 (in molar fractions).

Table 5.1. Ballistic factor $\beta_m = m/(A_{ref}C_D)$ of ballistic probes and lifting capsules.

Vehicle	Mass [kg]	A_{ref} [m ²]	Drag C_D	Ballistic factor β_m [kg/m ²]	Ref.
OREX	761.0	9.08	$\approx 1.40_{M=\infty}^{\alpha=0^\circ}$	60.0	[10, 11]
EDV No.3	42.9	0.7854	$0.9595_{M=\infty}^{\alpha=0^\circ}$	57.0	[12]
HUYGENS	≈ 300.0	5.73	$\approx 1.52_{M=\infty}^{\alpha=0^\circ}$	34.0	[13]–[15]
BEAGLE2	60.0	0.636	$\approx 1.45_{M=\infty}^{\alpha=0^\circ}$	65.0	[16, 17]
ARD	2, 800.0	6.16	$1.247_{M=10}^{\alpha=-22.8^\circ}$	365.0	[18]
APOLLO	5, 470.0	12.02	$1.247_{M=10}^{\alpha=-22.7^\circ}$	365.0	[19, 20]
VIKING type	9, 200.0	15.20	$1.391_{M=10}^{\alpha=-23.9^\circ}$	435.0	[21]

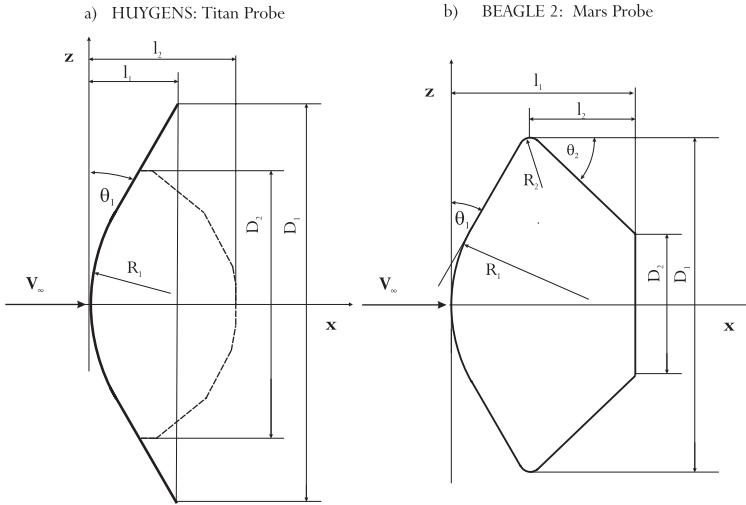


Fig. 5.3. Shape definition of the ballistic probes HUYGENS, [14, 15], and BEAGLE2, [16, 17]. HUYGENS has a rugged back contour which is idealized with a dashed line in the figure.

Table 5.2. Geometrical data and mission information of ballistic capsules.

Vehicle	Mission	v_e	l_1	l_2	D_1	D_2	R_1	R_2	θ_1	θ_2
		[km/s]	[mm]	[mm]	[mm]	[mm]	[mm]	[mm]	[°]	[°]
HUYGENS [14, 15]	Titan	6.0	620.5	985.0	2,700.0	1,790.0	1,250.0		30	
BEAGLE2 [16, 17]	Mars	5.63	499.5	212.0	900.0	371.8	417.0	29.0	30	43.75
OREX [10, 11]	Earth LEO	7.4	1,060.0		3,400.0	1,735.0	1,350.0	100.0	40	40

The geometrical definition of the HUYGENS probe is given in Fig. 5.3 a) and Table 5.2.

In the frame of a recent space mission to the planet Mars, the British small and low-cost probe BEAGLE2 was ejected from ESA's "Mars Express" (launched in June 2003) in order to conduct a ballistic entry into the Martian atmosphere. The capsule had a mass of 60 kg with a payload of 30 kg. Once having arrived at the Martian surface, a six-month scientific mission was planned to follow. The Martian atmosphere consists essentially of 97 per cent CO_2 , 3 per cent N_2 (in molar fractions) and a trace amount of Ar. Besides the

provision of a reliable aerodynamic data base for a safe landing on the surface, the determination of the thermal loads was the main task of the planned mission [16, 17]. Unfortunately, BEAGLE2 was lost without knowing the exact reasons. Figure 5.3 b) shows the shape of BEAGLE2.

The space program in Japan had the objective of developing an unmanned winged orbiter called HOPE. To reach this goal, several demonstrators were designed and developed for getting aerodynamic and aerothermal data (and data for other disciplines like flight mechanics and vehicle control) in real free-flight environments. The Orbital Re-entry Experiment OREX was one of these demonstrators. It had a successful flight in Earth orbit and a subsequent ballistic re-entry in February 1994. The main tasks of this flight were to test the reliability of the TPS system (which was that one developed for HOPE) and to collect data of the hypersonic and supersonic aerodynamic and aerothermal behavior. We give, without further discussion, the data of OREX in Table 5.2 and Fig. 5.4.

5.2.2 Lifting Capsules

Capsules flying with an $L/D > 0$ while entering an atmosphere are called lifting capsules. If they have an axisymmetric shape, their angle of attack necessarily must be negative in order to achieve positive lift, Section 5.3. Mission information about such RV-NW's, the American APOLLO and the Russian SOYUZ vehicle being the most prominent ones, is given in Table 5.3.

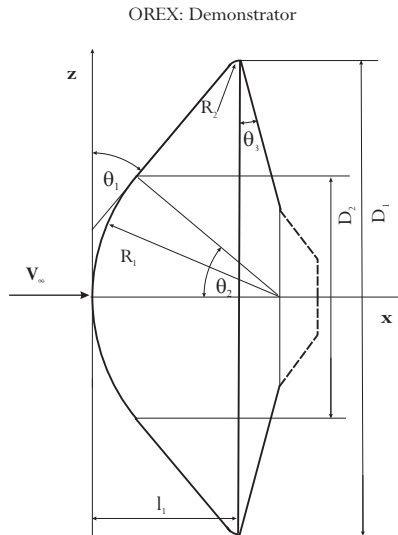


Fig. 5.4. Shape definition of the ballistic probe OREX, [10, 11].

There is no doubt that the aerothermodynamics of the APOLLO capsule are one of the best known. Due to the large number of flights in the 1960s and 1970s either in Earth orbit or of Lunar return, the free-flight data base is remarkable. During the design phase of APOLLO, most of the aerothermodynamic data was obtained from ground simulation facility experiments, [19, 20, 22, 28]–[30]. Heat transfer measurements in the hypersonic flow regime were conducted in “cold” hypersonic tunnels.

Some thirty years later in Europe, the Atmospheric Re-entry Demonstrator (ARD) was developed. Its shape was a sub-scaled APOLLO configuration with a modified rear part. In a first iteration, the aerodynamic data base for ARD was taken from APOLLO and later on improved. The advent of powerful numerical simulation methods had made it possible to strongly increase the understanding of complicated flow fields with multiple interactions of shocks, vortices and boundary layers, either attached or separated, with the influence of hot gases in thermodynamic equilibrium or non-equilibrium, with finite-rate catalytic wall conditions, and so on. Also new high-enthalpy facilities were available in Europe with the HEG in Germany and the F4 tunnel in France. These new capabilities were employed during the ARD’s development phase. ARD was successfully flown in October 1998 and was recovered in the Pacific Ocean [18, 23, 31]. In Fig. 5.5 the shapes of APOLLO and ARD are plotted, while the corresponding geometrical values are listed in Table 5.4.

The Russian lifting capsule SOYUZ was the space transportation system to the Russian space station MIR. Since year 2001, besides the US Space Shuttle System, SOYUZ is guaranteeing the access to the International Space Station (ISS). Further, it acts as a rescue vehicle for the Space Station crew in case of any injury or sickness of the crew members [24].

Table 5.3. Mission information of lifting capsules.

Vehicle	Mission	V_e [km/s]	Ref.
APOLLO	Earth LEO	7.67	[20, 22]
	Lunar return	10.76	
ARD	Earth LEO	7.4	[18, 23]
SOYUZ	Earth LEO	7.9	[24]
VIKING 1	Earth LEO	7.9	[25]
AFE	Earth GEO	10.36	[4]
	Mars entry	5.70	
CARINA	Earth LEO	7.6	[26, 27]

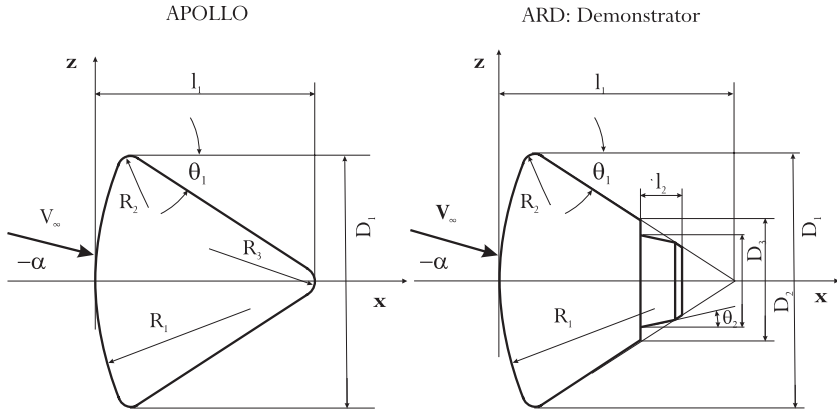


Fig. 5.5. Shape definitions of the lifting capsules APOLLO [20, 22] and ARD, [18, 23].

VIKING-type shapes are interesting configurations if non-winged solutions are sought for the transport of humans to and from space. In the frame of ESA’s post-HERMES Manned Space Transportation Programme (MSTP) and the Crew Transport Vehicle (CTV) activities, VIKING-type shapes were investigated in very large detail by wind tunnel experiments, approximate engineering methods and highly sophisticated numerical simulation methods, Fig. 5.6.

Since the beginning of the space era, discussions about the advantage of aeroassisted orbital transfer vehicles have taken place. To realize this technique requires a very good knowledge of the aerodynamic and aerothermal behavior of the vehicle with respect to performance and controllability as well as thermal

Table 5.4. Geometrical data of lifting capsules, Figs. 5.5 to 5.7.

Vehicle	l_1 [mm]	l_2 [mm]	l_3 [mm]	D_1 [mm]	D_2 [mm]	D_3 [mm]	R_1 [mm]	R_2 [mm]	R_3 [mm]	θ_1 [°]	θ_2 [°]
APOLLO	3,529.0			3,912.0			4,694.0	196.0	232.	33	
ARD	2,594.0	460.0		2,800.0	1,317.0	1,015.	3,360.0	140.0		33	12
SOYUZ	2,142.0	1,778.	936.	2,200.0	980.0		2,235.0	978.0		11	7
VIKING 1	3,740.0			4,400.0			2,200.0	88.0		80	25
AFE	376.0			4,267.0						30	17
CARINA	1,263.0	482.0		1,078.0	634.0		4,380.0	2,124.0		13	

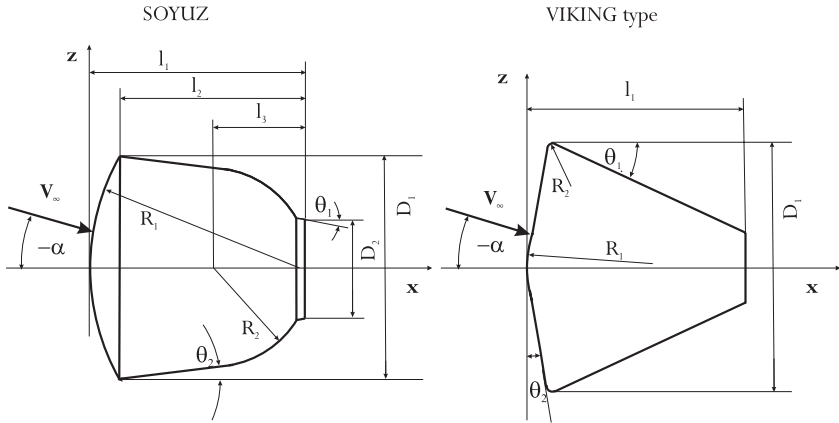


Fig. 5.6. Shape definitions of lifting capsules SOYUZ [24] and VIKING type [25].

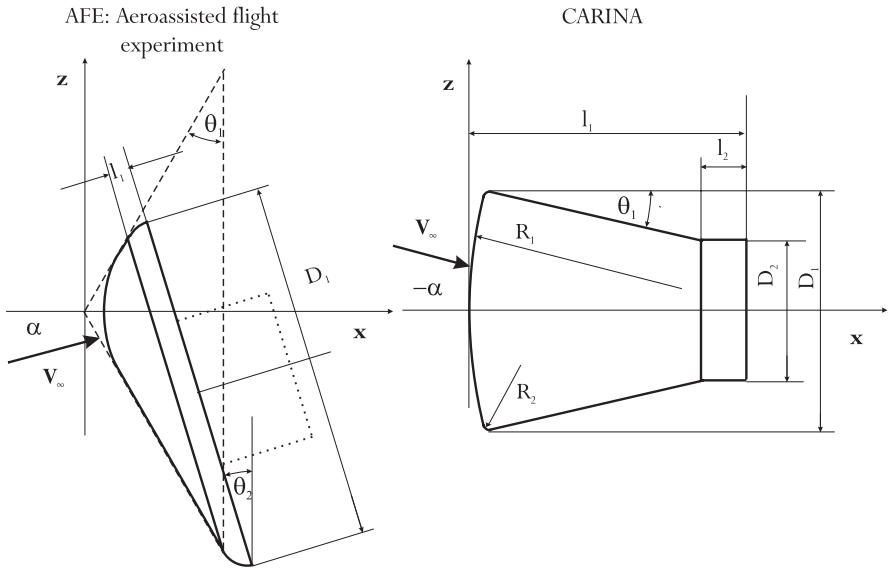


Fig. 5.7. Shape definitions of lifting capsules AFE [3, 32, 33], and CARINA [26].

loads. As was already mentioned, in order to improve the existing data bases in this regard, NASA had started in the 1980s a project with a generic configuration called Aeroassisted Flight Experiment (AFE), Fig. 5.7. Due to the asymmetric shape of AFE, the aerodynamic performance with $0.25 \lesssim L/D \lesssim 0.3$ is reached for a trim angle of attack $\alpha_{trim} \approx 0^\circ$ with respect to the x -coordinate.

The expected advantages of this shape are twofold. First, an impingement of the shear layer on the payload, located behind the heat shield, is more un-

likely for moderate angle of attack variations or it happens farther downstream of the base compared to axisymmetric bodies. Secondly, the heating at the shoulders of the front shield, often the peak heating regime, is lower for AFE ($\alpha_{trim} \approx 0^\circ$) due to the larger radii at the shoulders than for axisymmetric shapes with trim angles $\alpha_{trim} \approx -20^\circ$.

The main goal of the aeroassisted orbital transfer technique is to reduce the relative orbital speed with the help of the atmosphere if for example an orbit transfer (from geostationary to low Earth orbit) or an atmospheric re-entry with supersonic speed (Lunar return) has to be conducted. The advantage of this process, today called aerocapturing, Sub-Section 5.1.2, is the possibility to dramatically decrease (up to 50 per cent) the total orbiter mass. This is mainly due to the fact that no (or a reduced) chemical propulsion system including the propellant, is needed compared to conventional missions.

Since the beginning of this century, there is a renewed interest in this technique in the frame of Mars exploration activities, where a Mars Sample Return Orbiter (MSRO) which has an AFE-like shape was generically defined and investigated in detail. The realization of this project (later than the year 2013 according to ESA's exploration plan) would be the first aerocapturing mission ever performed [3, 34].

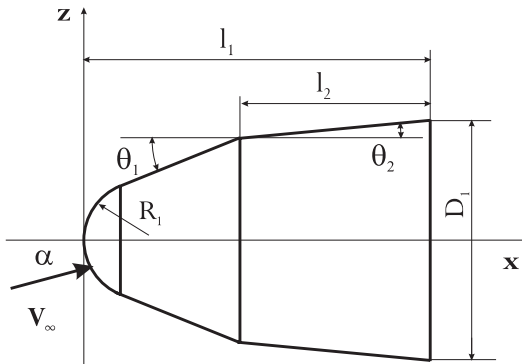
In the 1990s, the Italian Space Agency (ASI) supported a satellite project named Capsula di Rientro Non Abitata (CARINA) for performing microgravity experiments in space. This system has the capability for atmospheric re-entry. The re-entry module of this system had a configuration based on the APOLLO/GEMINI shape and should have been able to return a payload mass of about 130 kg, Fig. 5.7 (right). An aerodynamic data base was established for the transonic through hypersonic Mach number range [26, 27].

5.2.3 Bicones

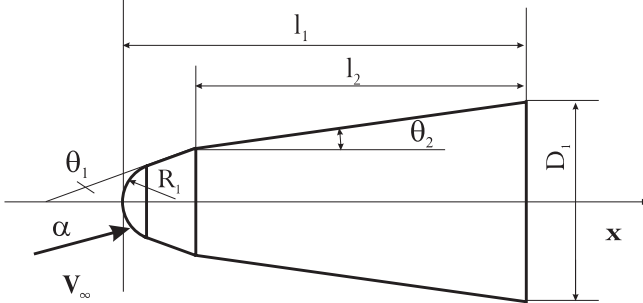
Since a long time, various bicones, fat (bluff) bicones, slender bicones, bent bicones, Fig. 5.8, were considered for particular space missions and some preliminary studies have been made. The advantage of these configurations is the higher lift-to-drag ratio L/D compared to simple capsules. Fat bicones have a $L/D \approx 0.6$, slender ones a $L/D \approx 0.9$ and bent bicones with even higher values of up to $L/D \approx 1.4$.² In contrast to the classical axisymmetric RV-NW's, these shapes achieve lift with a positive angle of attack. (Orbital transfer operations, where only the altitude of the orbit is changed, may be feasible with vehicles with a $L/D \approx 0.3$, but for missions with a change of the inclination of the target orbit, higher aerodynamic performance is necessary during the aerocapturing phase.) In general, bicones are appropriate for missions where a large cross-range capability, good maneuverability, low landing distortion (vehicle recovery), low entry loads are required, and for high entry velocities and thin atmospheres (low deceleration).

² The US Shuttle has a $L/D \approx O(1)$, Chapter 3.

a) Bluff bicone (Dasa , CTV)



b) Slender bicone (Tsniimash)



c) Bent bicone

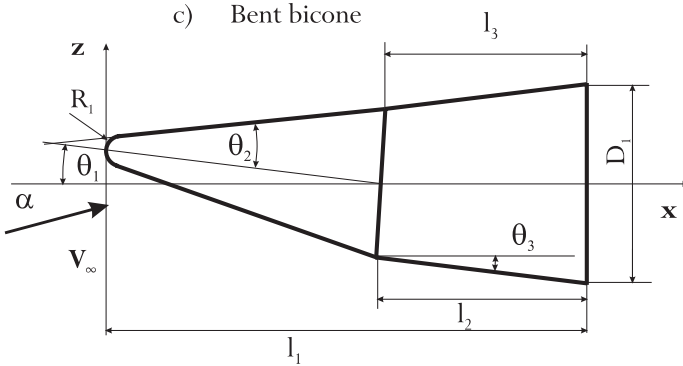


Fig. 5.8. Shape definitions of a) fat (bluff) bicone [36], b) slender bicone [24], and c) bent bicone [37].

Table 5.5. Geometrical data and mission information of bicones.

Vehicle	Mission	v_e	l_1	l_2	l_3	D_1	R_1	θ_1	θ_2	θ_3
		[km/s]	[mm]	[mm]	[mm]	[mm]	[mm]	[°]	[°]	[°]
CTV DASA [36]	Earth LEO	7.6	6,300.0	3,425.0		4,400.0	1,056.0	22	5.4	
CTV ESA [24]	Earth LEO	7.6	6,830.0	3,745.0		4,398.0	882.0	20	7	
Slender Bicone [24]	Earth LEO	7.6	8,395.0	6,863.0		4,159.0	796.0	20	8	
Bent Bicone ³ [35], [37]	Earth LEO	7.6	182.52	80.85	77.32	76.20	5.79	7	12.84	7

Up to now none of these vehicles have reached a development state for performing a free flight (neither orbital nor suborbital). Some American reports inform about investigations in this field [35, 37]. In Europe several activities were performed in the frame of ESA's Crew Transport Vehicle (CTV) studies, [1, 36]. Also in Russia, there are some preliminary studies on biconic shapes [24]. Three of these biconic shapes can be found in Fig. 5.8 and the geometrical parameters are listed in Table 5.5.

5.3 Trim Conditions and Static Stability of RV-NW's

In this Section, we discuss the aerodynamic capabilities and potentials of various non-winged vehicles. For this, it is necessary to define the coordinate systems applied including those for the aerodynamic forces and moments, and to show what trim conditions and static stability mean. General formulas and definitions describing the aerodynamic state of all kind of vehicles are found in Chapter 7.

5.3.1 Park's Formula

For capsule-like shapes at supersonic and hypersonic Mach numbers and different angles of attack, it is observed that the line of action of the resultant aerodynamic force crosses the axis of symmetry (namely the x -coordinate) approximately at the same position. This intersection point is called the metacenter x_{cp} , Fig. 5.9. In cases where the aerodynamic coefficients are known for a few discrete angles of attack, this observation can be helpful for determining the

³ The data of the bent bicone are those of a wind tunnel model.

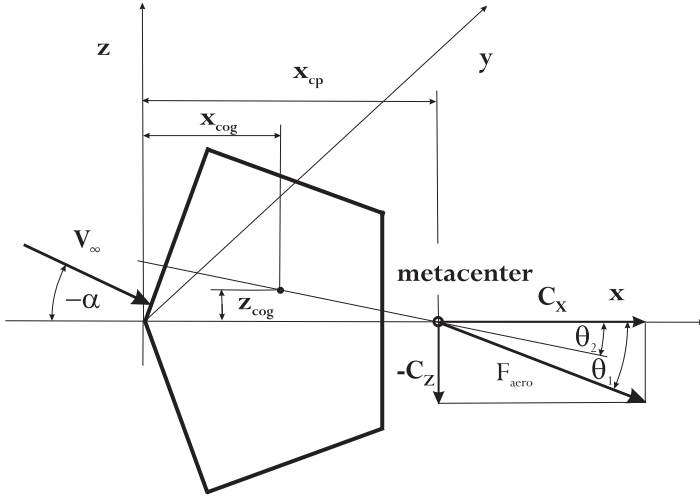


Fig. 5.9. Definition of the metacenter.

trim angle of attack. This is often the situation, if the aerodynamic data are obtained with the help of numerical simulation methods, where non-equilibrium thermodynamics, catalytic walls, turbulent flow, etc., are taken into account, which makes the computations (still) very expensive and time consuming.

We assume that x_{cp} and the force coefficients C_X and C_Z are nearly independent of α (for $M_\infty \gtrsim 2$) and $\partial C_m / \partial \alpha$ is approximately constant.⁴ With eq. (7.2), we can write

$$L_{ref} C_m(\alpha_j)|_{cog} - C_Z(\alpha_j)(x_{cog} - x_{cp}) + C_X(\alpha_j)z_{cog} = 0, \quad z_{cp} = 0, \quad (5.2)$$

$$C_m(\alpha_{trim})|_{cog} = 0, \quad (5.3)$$

$$C_m(\alpha_j)|_{cog} + (\alpha_{trim} - \alpha_j) \frac{\partial C_m(\alpha_j)}{\partial \alpha} = 0, \quad (5.4)$$

$$- \left\{ \frac{L_{ref} \alpha_j}{C_Z(x_{cog} - x_{cp})} \frac{\partial C_m(\alpha_j)}{\partial \alpha} \left(\frac{\alpha_{trim}}{\alpha_j} - 1 \right) + 1 \right\} \frac{C_Z(\alpha_j)}{C_X(\alpha_j)} + \frac{z_{cog}}{x_{cog} - x_{cp}} = 0. \quad (5.5)$$

In these equations α_{trim} denotes the trim angle of attack and α_j the angle of attack, where the aerodynamic coefficients are known. Further we obtain from eq. (7.14):

$$- L_{ref} \alpha_j \frac{\partial C_m(\alpha_j)}{\partial \alpha} = - \alpha_j \frac{\partial C_Z(\alpha_j)}{\partial \alpha} (x_{cog} - x_{cp}) + \alpha_j \frac{\partial C_X(\alpha_j)}{\partial \alpha} z_{cog}. \quad (5.6)$$

⁴ This holds, for instance, for the VIKING 2 shape, Fig. 5.10, and also some others in the following sub-section.

With $\alpha_j \partial C_Z(\alpha_j)/\partial \alpha \approx C_Z$, $\partial C_X(\alpha_j)/\partial \alpha \approx 0$, $\tan \theta_1 = C_Z/C_X$, and $\tan \theta_2 = z_{cog}/(x_{cp} - x_{cog})$, finally eq. (5.5) has the form

$$\alpha_{trim} = -\alpha_j \frac{\tan \theta_2}{\tan \theta_1}. \quad (5.7)$$

This is Park's formula [38, 39], which allows the trim angle of attack to be found from aerodynamic coefficients given at a discrete trajectory point in a suitable vicinity of the trim angle. Later in this chapter we will demonstrate the applicability of this formula by some examples.

5.3.2 Performance Data of Lifting Capsules

In this Sub-Section we give an overview about aerodynamic coefficients of some of the shapes presented in Section 5.2.⁵ Since most of the shapes are bodies of revolution (the AFE shape is considered only for the yaw angle $\beta = 0$) the coefficients $C_X, C_Z, C_m, L/D$ describe the aerodynamic performance, Fig. 7.3. The coefficient for the dynamic stability $C_{mq} + C_{m\dot{\alpha}}$ will be treated separately in Section 5.4.

The configurations of VIKING-type shapes are characterized by the following geometrical relations: $R_1/D_1, R_2/D_1, l_1/D_1, \theta_1, \theta_2$. The values of the VIKING 1 shape are $R_1/D_1 = 0.5, R_2/D_1 = 0.02, l_1/D_1 = 0.85, \theta_1 = 80^\circ, \theta_2 = 25^\circ$, Fig. 5.6. VIKING 2 has a different aft cone angle with $\theta_2 = 20^\circ$ and the reference diameter $D_1 = L_{ref} = 4,400$ mm [21].

Aerodynamic data of the VIKING 2 shape are given in Fig. 5.10. Note, as mentioned above, capsules have a positive lift only for negative angle of attack. Therefore all coefficients are plotted versus negative angles of attack. Further, the conventions of the signs are defined by Fig. 7.3. The data of Fig. 5.10 are taken for $0.5 \leq M_\infty \leq 3.97$ from wind tunnel experiments. The $M_\infty = 10$ values are based on Euler calculations with the perfect gas assumption, while for $M_\infty = 19$, an Euler computation is used with a non-equilibrium real gas. Since the trim angle of attack varies between $\alpha_{trim} \approx -10^\circ$ ($M_\infty = 0.5$) and $\alpha_{trim} \approx -25^\circ$ ($M_\infty = 19$), it seems possible to fly in the whole Mach number range with L/D between 0.2 and 0.4.

All the aerodynamic coefficients plotted in Fig. 5.10 exhibit non-monotonic behavior with regard to the Mach number with extreme values in the transonic regime. However, for $M_\infty \geq 3.97$ there exists a near Mach number independence for C_Z, C_m and L/D which, however, is not so clear for C_X . Finally, for the reference point chosen, the capsule is statically stable in the whole Mach number and angle of attack regime, since the condition $C_{m\alpha} < 0$ is met everywhere, see Fig. 7.9.

⁵ The reader should note the custom in RV-NW aerodynamics, that the integral aerodynamic forces and coefficients are given in terms of the axial force X and the normal force Z (body axis system). For the transformation into the flight path system see Section 7.6.

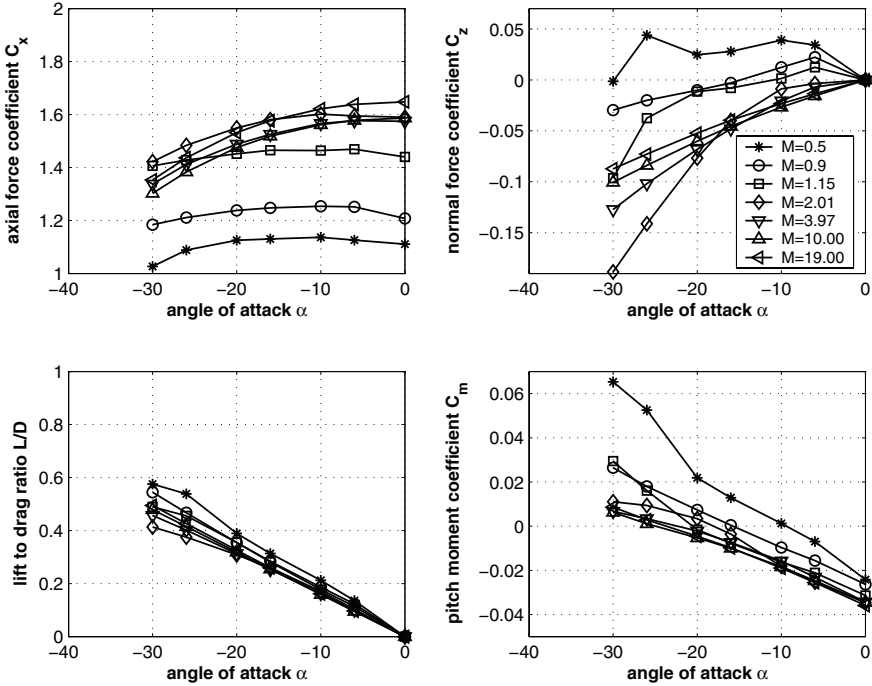


Fig. 5.10. Aerodynamic data of the VIKING 2 shape. Moment reference: $x_{ref} = 0.34D_1$, $z_{ref} = 0.0218D_1$. Data source: [21].

Figure 5.11 shows the aerodynamics of the APOLLO capsule. This shape produces L/D values which are dependent on the Mach number in a similar way as the VIKING-type shapes with realistic values of L/D in the range of 0.3, [40, 41]. The variation of the trim angles for the various Mach numbers is in the same range as for the VIKING 2 shape. Again static stability is preserved in the whole Mach number regime.

Another famous capsule, besides APOLLO, is the Russian SOYUZ. It is the vehicle which serves the ISS. It is of interest to see the relatively large spread of the L/D values with respect to the Mach number, Fig. 5.12. This data set is completely generated by wind tunnel results and the plotted values are taken from [24]. The highest Mach number measured is $M_\infty = 5.96$. It is not clear if apparent changes of the aerodynamic coefficients will occur for hypersonic Mach numbers up to 30, but a look at the data for VIKING 2 or APOLLO reveals that the differences are probably low. Thus, SOYUZ is able to fly in the hypersonic regime with $L/D \approx 0.3$ for a trim angle $\alpha_{trim} \approx -26^\circ$. A further increase of the aerodynamic performance (i.e., higher L/D) seems hardly possible, whatever the z_{offset} of the center-of-gravity is, Sub-Section 5.3.3. Static stability is given for all the Mach numbers tested. Comparing the three vehi-

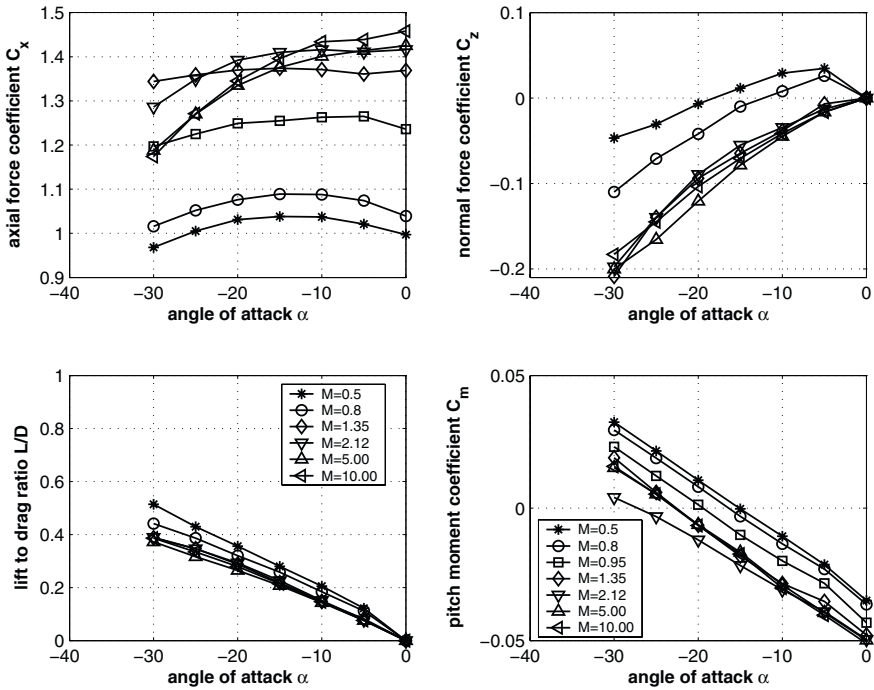


Fig. 5.11. Aerodynamic data of the APOLLO shape. Moment reference: $x_{ref} = 0.265 D_1, z_{ref} = 0.035 D_1$. C_m and C_X , as well as L/D and C_Z have the same legend. Data source: [40].

cles discussed above, the VIKING 2 shape has obviously the best potential in aerodynamic performance, but this shape was never flown as a manned space transporter.

The AFE has an interesting non-axisymmetric shape, Fig. 5.7. About ten years after the respective NASA technology program in the late 1980s and the beginning 1990s (see above), a renewed interest in this shape arose at the European Space Agency (ESA) in the frame of the Mars Sample Return Orbiter (MSRO) activities. The original shape had a diameter of $D_1 = 4,267\text{mm} \hat{=} 14\text{ft}$ which was reduced in the MSRO case to $D_1 = 3,657\text{mm} \hat{=} 12\text{ft}$. Figure 5.13 shows C_X, C_Z, C_m and L/D for some hypersonic Mach numbers.

The $M_\infty = 11.8$ experiments were conducted in the Hypervelocity Free-Flight Aerodynamic Facility (HFFAF) at NASA Ames [42]. From the experimental conditions, it seems that this facility is able to duplicate nearly all the parameters of a real hypersonic free-flight, namely, the free-stream pressure, density and temperature, as well as the velocity. Therefore one could expect that the data reflect properly the influence of the real gas behavior, if Mach number independence exists, Section 3.6. On the other hand, the data reduc-

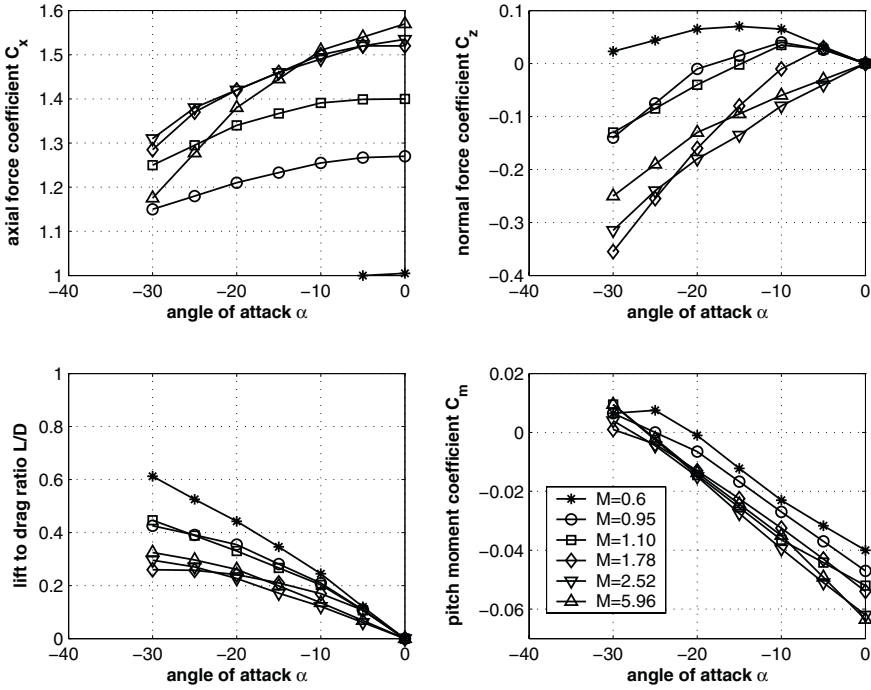


Fig. 5.12. Aerodynamic data of the SOYUZ shape. Moment reference: $x_{ref} = 0.370 D_1$, $z_{ref} = 0.039 D_1$. Data source: [24].

tion requires the flight-mechanical evaluation of the trajectory of the model inside the facility, which is obviously not a simple task [42].

Further for $M_\infty = 5.94$ and 9.55 , data were measured in NASA Langley’s cold hypersonic wind tunnel [43]. The Langley data are close together for both Mach numbers. The pitching moment is larger for the Langley data compared to the HFFAF data, which was not expected, since at least for axisymmetric shapes, real gas effects normally increase the pitching moment and increase the magnitude of the trim angle.

The pitching moment of a complete non-equilibrium CFD solution (for the Martian atmosphere) for $M_\infty = 18.7$ and $\alpha = -4^\circ$ is given in [44] and is plotted in Fig. 5.13, lower right. The values are closer to Langley’s data. Nevertheless, other numerical investigations [3] show that in the hypersonic flight regime, the trim angle would be approximately -1° , which is in a better agreement with the HFFAF data than the Langley data.

From the above discussion and that one from Sub-Section 5.3.7 about the influence of real gas effects, we note two points:

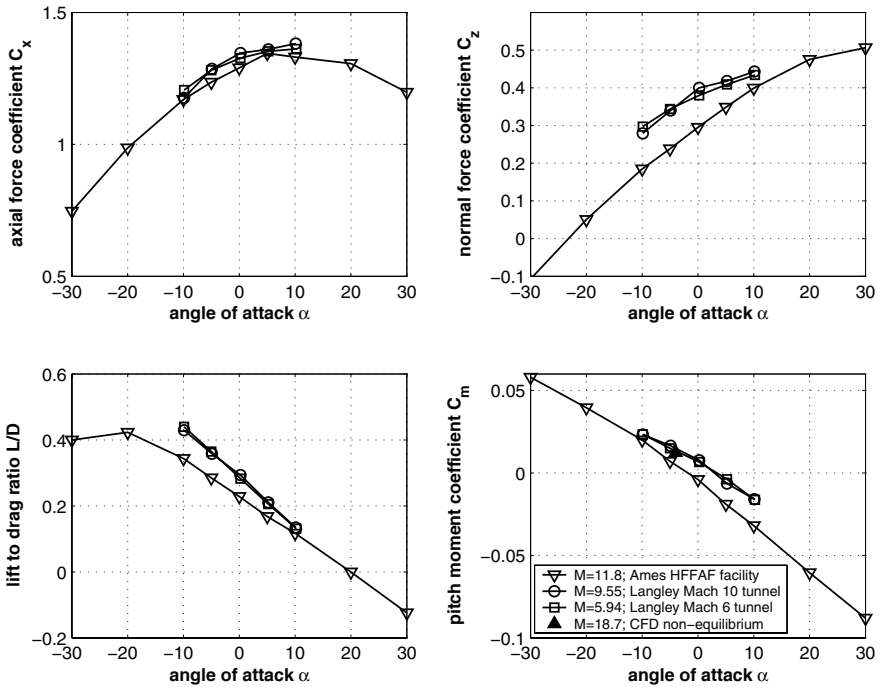


Fig. 5.13. Aerodynamic coefficients in the hypersonic flow regime for the AFE shape. Moment reference: $x_{ref} = 0.2509 D_1$, $z_{ref} = -0.2301 D_1$, measured from the origin. Data source: [42, 43].

- There is a high temperature, real gas effect on the trim angle.
- Ground facility simulation seems to be very difficult. CFD methods with the most advanced thermodynamic models, if properly validated, offer the most promising results.

5.3.3 Controlled Flight and the Role of the Center-of-Gravity

Every non-winged vehicle with an axisymmetric shape is only able to conduct a lift-based, trimmed flight if a z -offset of the center-of-gravity exists. Otherwise the trim angle of attack is zero, leading to zero lift and lift-to-drag ratio.

To discuss this in more detail, we use the aerodynamic data of the VIKING 2 shape, Fig. 5.10. From the lift-to-drag graph, we can extract that a hypersonic performance of $L/D = 0.3$ can be achieved by a trim angle of $\alpha_{trim, L/D=0.3} = -17.8^\circ$ and $L/D = 0.4$ by $\alpha_{trim, L/D=0.4} = -23.8^\circ$. With the help of eq. (7.11) we can determine all the positions of the center-of-gravity ensuring trimmed flight with a fixed L/D after the coordinates of the center-of-pressure have been

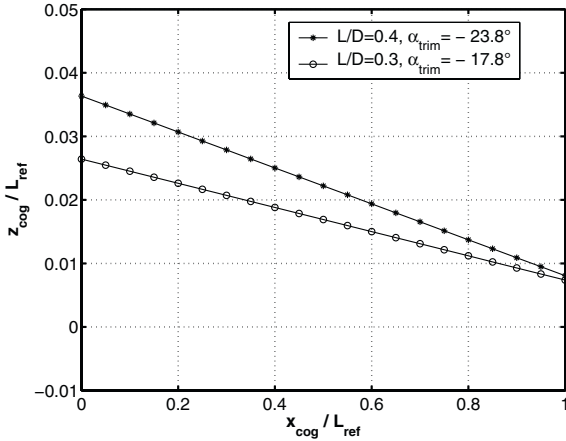


Fig. 5.14. Center-of-gravity positions for two trim conditions of the VIKING 2 shape.

determined by means of the corresponding ones of eqs. (7.5) to (7.10). In Fig. 5.14 the resulting “center-of-gravity lines” for the two design points are shown.

It should be mentioned here that the free-flight, hypersonic experience of the APOLLO capsule exhibited a trim angle that was approximately 3° lower than predicted, with the consequence of a lower L/D value. In the frame of ESA’s MSTP, this phenomenon was investigated in great detail on the ARD capsule which has nearly the same aerodynamic properties as the APOLLO capsule, Fig. 5.5. The outcome was that mainly the extreme heating of the air in the shock layer in front of the vehicle is responsible for this behavior. This heating leads to the excitation of vibrational modes in the molecules, to dissociation and partial ionization (for entry speeds of $v_e \gtrsim 8$ km/s). The thermodynamic state can then be in equilibrium or non-equilibrium, depending on the ambient density, which influences the surface pressure distribution. This behavior is summarized by the term “high temperature real gas effects” and will be treated in more detail in Sub-Section 5.3.7.

It is evident from eq. (7.11) that for $C_X/C_Z \gg 1$ the relation $z_{cog}/x_{cog} \ll 1$ holds. Therefore the z-offset of the center-of-gravity z_{cog} is the dominating quantity for ensuring flyability and controllability. Its influence on the trim angle of attack and on L/D is very high, which is distinctly demonstrated in Fig. 5.15.

A change of 1 per cent in $z_{offset} \equiv z_{cog}$ (this is only 44 mm for the VIKING 2 vehicle) alters the trim angle of attack by about $\Delta\alpha_{trim} \approx 9^\circ$. On the other hand changes in the x-coordinate of the center-of-gravity x_{cog} influence the trim angle only slightly, which can be concluded from Fig. 5.16. A shift of 15 per cent of the moment reference $x_{ref} \equiv x_{cog}$ (in our example 660 mm) leads to a trim angle change of merely $\Delta\alpha_{trim} \approx 2^\circ$.

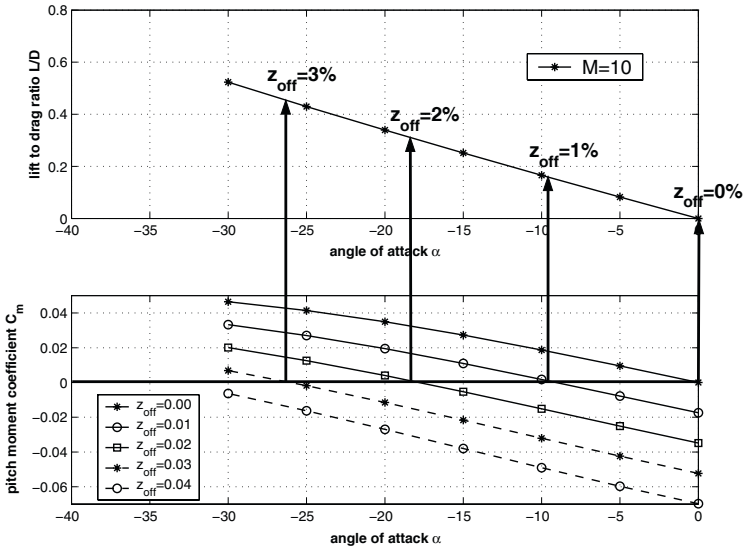


Fig. 5.15. Influence of $z_{offset} \equiv z_{cog}$ on aerodynamic trim for the VIKING 2 shape; $z_{offset} \equiv z_{off}$ is given in per cent of the reference length $L_{ref} = D_1 = 4,400$ mm.

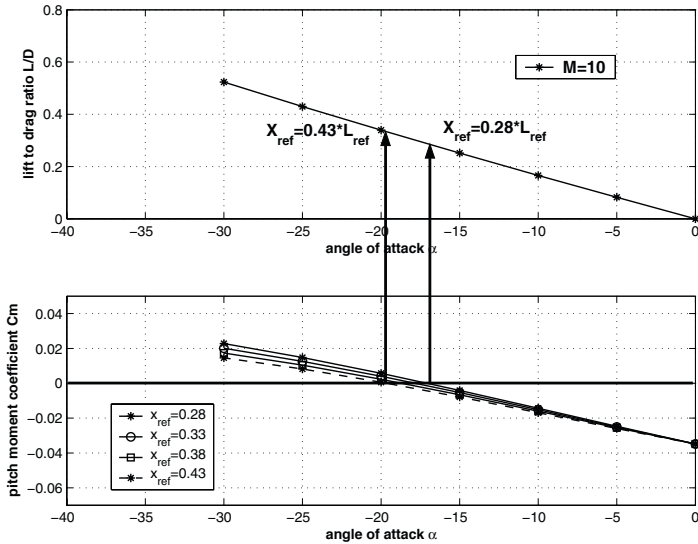


Fig. 5.16. Influence of $x_{ref} \equiv x_{cog}$ on aerodynamic trim for the VIKING 2 shape; $L_{ref} = D_1 = 4,400$ mm.

5.3.4 Sensitivity of Aerodynamics against Shape Variations

It is important to understand what effects that contour changes of a capsule may produce. We demonstrate this with the VIKING 3 as baseline shape. The geometrical relations in this case are $R_1/D_1 = 0.5$, $R_2/D_1 = 0.02$, $l_1/D_1 = 0.95$, $\theta_1 = 80^\circ$, $\theta_2 = 16^\circ$ (see Fig. 5.6 with $\theta_2 = 16^\circ$). The investigation is valid for hypersonic flow conditions [45]. The moment reference point is given by $x_{ref} = 0.33 L_{ref}$, $z_{ref} = 0.02 L_{ref}$ for all the pitching moment diagrams.

R_1/D_1 Variation

The influence of R_1/D_1 variations on the aerodynamic performance is rather weak and always $\Delta(L/D) \lesssim 1$ per cent. However, R_1 should have a reasonably large value, since the thermal loads are directly related to the inverse of the square root of R_1 .

R_2/D_1 Variation

Let us consider what happens if R_2/D_1 is increased to 0.1, Fig. 5.17. First, a remarkable decrease in the aerodynamic performance L/D can be observed and, secondly, the pitching moment increases, which results in a trim angle shift of roughly 3.5° ($\alpha_{trim, R_2/D_1=0.02} \approx -20^\circ \implies \alpha_{trim, R_2/D_1=0.10} \approx -16.5^\circ$).

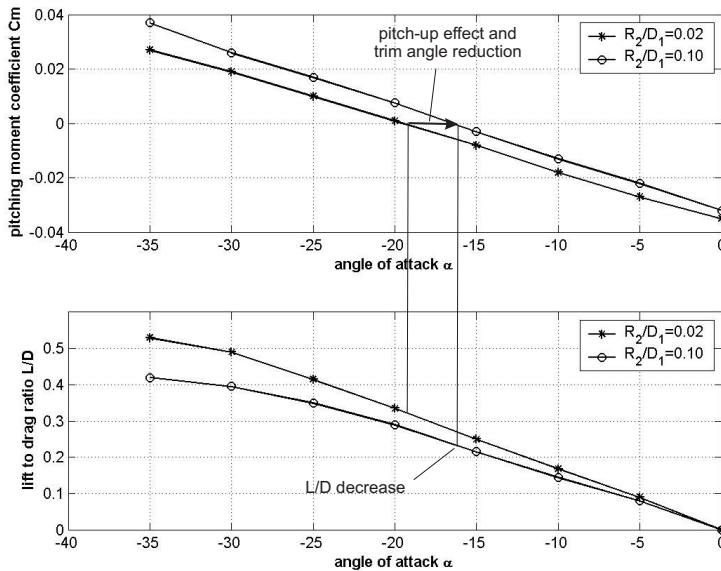


Fig. 5.17. Influence of R_2/D_1 on aerodynamic coefficients based on the VIKING 3 shape. Data source: [45].

The pitching moment increase means that a pitch-up effect occurs. The static stability is seen to be slightly increased with $|\partial C_m/\partial \alpha|_{R_2/D_1=0.1} > |\partial C_m/\partial \alpha|_{R_2/D_1=0.02}$ [25]. Moreover, the thermal loads at the shoulder are reduced for $R_2/D_1 = 0.1$ due to the diminished flow expansion there compared to the $R_2/D_1 = 0.02$ case.

Physical Explanation

The increase of R_2/D_1 can be considered as a reduction of bluntness of the capsule. The axial force is considerably diminished due to this reduction, which reduces the lift L and thus L/D . The pressure force on the leeward side is reduced more than that on the windward side which leads to a pitch-up effect. This result is confirmed by [46], where a 70° spherical cone with different shoulder radii is investigated by employing a numerical method solving the Euler equations.

l_1/D_1 Variation

The influence of changing l_1/D_1 from 0.85 to 1.05 is investigated. While L/D is nearly the same for $l_1/D_1 = 0.85$ and 1.05, the pitching moment is higher for $l_1/D_1 = 0.85$ compared to $l_1/D_1 = 1.05$, which leads to a reduced trim angle α_{trim} , Fig. 5.18.

θ_1 Variation

The half cone angle θ_1 determines the magnitude of L/D , which grows with increasing θ_1 . To achieve a value of $L/D \approx 0.3$, a minimum of $\theta_1 = 60^\circ$ is required [32]. Further, the trim angle α_{trim} is decreased with increasing θ_1 , which is due to the fact that the center-of-pressure moves downstream. This results in a rise of the pitching moment. In an example given in [32], θ_1 was changed from 70° to 75° , which has caused a reduction in the magnitude of the trim angle α_{trim} from -20.8° to -19.5° .

θ_2 Variation

The variation $14^\circ \leq \theta_2 \leq 18^\circ$ is investigated [25]. For $\alpha < -20^\circ$ the pitching moment decreases slightly and L/D increases when θ_2 increases. For higher values of θ_2 this effect is shifted to higher angles of attack.

Physical Explanation

The increase of the aft cone angle θ_2 leads to an increase of the negative normal force coefficient C_Z , which reduces the lift. The flow past shapes with lower θ_2 values “sees” earlier the aft cone part, producing this negative C_Z increase, which on the other hand, brings an increase of the pitch-up effect, Fig. 5.19.

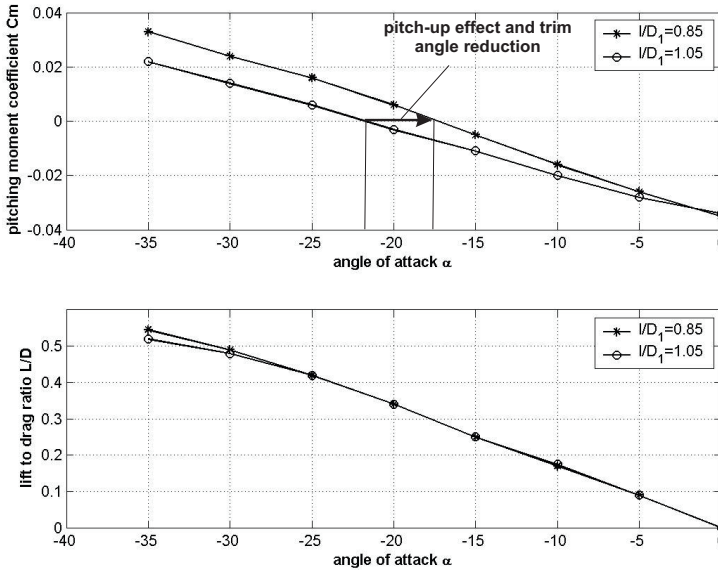


Fig. 5.18. Influence of l_1/D_1 on aerodynamic coefficients based on the VIKING 3 shape. Data source: [45].

5.3.5 Parasite Trim

During the development and testing of the classical capsules APOLLO and SOYUZ, it was observed over an angle of attack range $0^\circ \geq \alpha \geq -360^\circ$ that the pitching moment C_m could meet the trim and stability conditions ($C_m = 0$, $\partial C_m / \partial \alpha < 0$) also at other points besides the nominal one. These points are called “parasite trim points.” There are at least three reasons why the vehicle must be prevented from entering into such non-nominal trim positions:

- the re-entry process can only be successfully conducted with the heat shield pointing forward in order to cope with the mechanical and thermal loads,
- the parachute landing system can be deployed only if the apex cover can be jettisoned properly, which requires the heat shield pointing forward,
- in the launch abort case the escape procedure requires definitely a capsule heat shield in pointing-forward attitude.

The best solution of this problem would be given by a change to a vehicle shape which prevents the existence of parasite trim points. During the APOLLO program, a lot of tests were done with keels, spoilers and strakes, but obviously none of these devices did solve the problem satisfactorily [19, 22].

A typical C_m plot showing one parasite trim point (VIKING 2 shape) is given in Fig. 5.20. The nominal trim point is at $\alpha_{trim, nominal} = -7.9^\circ$, while the parasite trim point has the value $\alpha_{trim, parasite} = -141^\circ$.

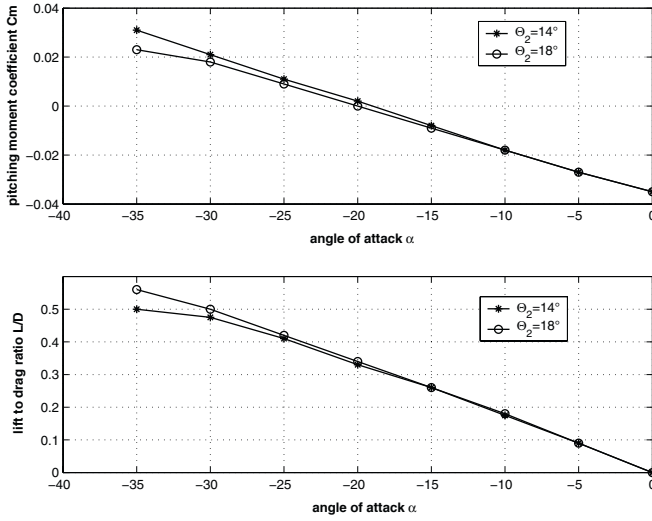


Fig. 5.19. Influence of θ_2 on aerodynamic coefficients based on the VIKING 3 shape. Data source: [25].

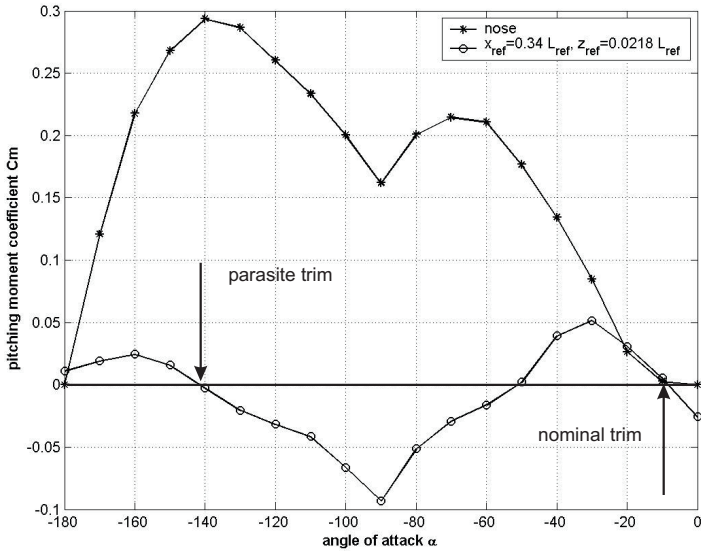


Fig. 5.20. Pitching moment of the VIKING 2 shape showing a parasite trim point for $M_\infty = 0.7$ (nose: $x_{ref} = 0, z_{ref} = 0$). Data source: [21].

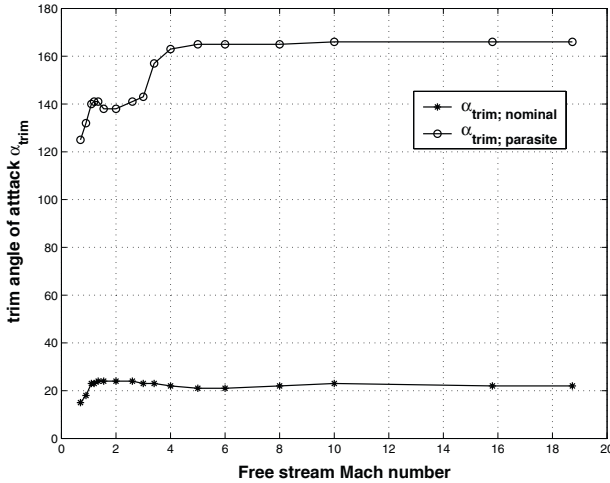


Fig. 5.21. APOLLO nominal and parasite trim points as function of Mach number. Data source: [22].

The APOLLO capsule possesses one parasite trim point over the whole Mach number range, which is somewhat fluctuating in the subsonic, transonic and low supersonic regimes. For higher Mach numbers, this trim point becomes independent of the Mach number, Fig. 5.21. This is valid for the center-of-gravity location $x_{cog}/D_1 = 0.657$ (measured from the apex) and $z_{cog}/D_1 = 0.035$.

The data available give hints that at least three parameters may influence the number and the location of parasite trim points. The first one is the x -component of the center-of-gravity. The larger x_{cog} , i.e., the more the center-of-gravity lies away from the apex, the more likely is the appearance of one or more parasite trim points or, the other way around, with an appropriately low x_{cog} value the appearance of these points can be avoided. Secondly, the Reynolds number has an influence. For larger Reynolds numbers one can often observe more than one parasite trim point, the reasons for this are not clear. The third parameter having an influence is the flight Mach number, again for not clear reasons. The lower the flight Mach number, the higher is the probability of the occurrence of parasite trim points. In Table 5.6 data are listed for SOYUZ and the VIKING 2 shape demonstrating this behavior.

5.3.6 Performance Data of Bicones

An alternative to the classical capsules are the bicones which can provide more than twice the lift-to-drag ratio L/D compared to those of capsules. Constraints of the internal lay-out (payload accommodation) and of the launch system (faring restrictions) may lead to a fat bicone shape like the one shown in Fig. 5.8 a). For this shape the L/D in hypersonic flight is approximately 0.65.

Table 5.6. Appearance of parasite trim points depending on center-of-gravity position and Reynolds number; x_{cog} and z_{cog} are non-dimensionalized with L_{ref} .

Vehicle	M_∞	x_{cog}	z_{cog}	$\alpha_{trim,nominal}$	$\alpha_{trim,parasite}$	Source of data
SOYUZ	1.10	0.30	0.0357	-22°	none	wind tunnel [24]
		0.45	0.0204	-18°	-132°	
VIKING 2	∞	0.30	0.0230	-23°	none	engineering methods [47]
		0.375	0.0205	-23°	-174°	
VIKING 2	0.70	0.34	0.0218	-7.9°	-141°	wind tunnel [21]
				-13.26°	-121° (1) $+122^\circ$ (2) $+146^\circ$ (3)	

As already mentioned, axisymmetric bodies can only be trimmed if the center-of-gravity is off the axis of symmetry. For the moment reference point applied here, Fig. 5.22, with $z_{ref} = 0 L_{ref}$ the vehicle is stable in the supersonic and hypersonic regime and unstable in the subsonic and the transonic regime, but cannot be trimmed, because for all Mach numbers $C_m \neq 0$ at $\alpha > 0$.

This problem can be overcome either by a suitable selection of the center-of-gravity (which may be restricted by the internal lay-out of the vehicle) or by employing aerodynamic devices like flaps and brakes (which complicates the design and the control system). The data set plotted in Fig. 5.22 was established by applying approximate methods like the local inclination methods for supersonic and hypersonic Mach numbers and panel methods for subsonic Mach numbers [48]. For all the aerodynamic coefficients, the Mach number dependency is clearly non-monotonic with extreme values in the transonic regime, as was already discussed for the capsules in Sub-Section 5.3.2. The coefficients approach Mach number independence for $M_\infty \gtrsim 5$.

For two points ($M_\infty = 1.5$, $\alpha = 20^\circ$ and 25°), Euler solutions were generated with the method reported in [49, 50]. As one can see, the agreement with the other data in Fig. 5.22 is rather good (except for C_X at $\alpha = 25^\circ$), which proves the reliability of the engineering method used. To get a bit more insight into the general flow field, the Mach number isolines (left) and the wall pressure distribution (right) are plotted in Fig. 5.23 for $M_\infty = 1.5$, $\alpha = 20^\circ$.

It is interesting to observe in the left part of the figure (Mach number isolines), the embedded shock on the leeward (upper) side at $x/L \approx 0.25$, which is generated due to an overexpansion of the flow (the wall pressure does not correspond to the cone deflection!), which can only be restored in supersonic

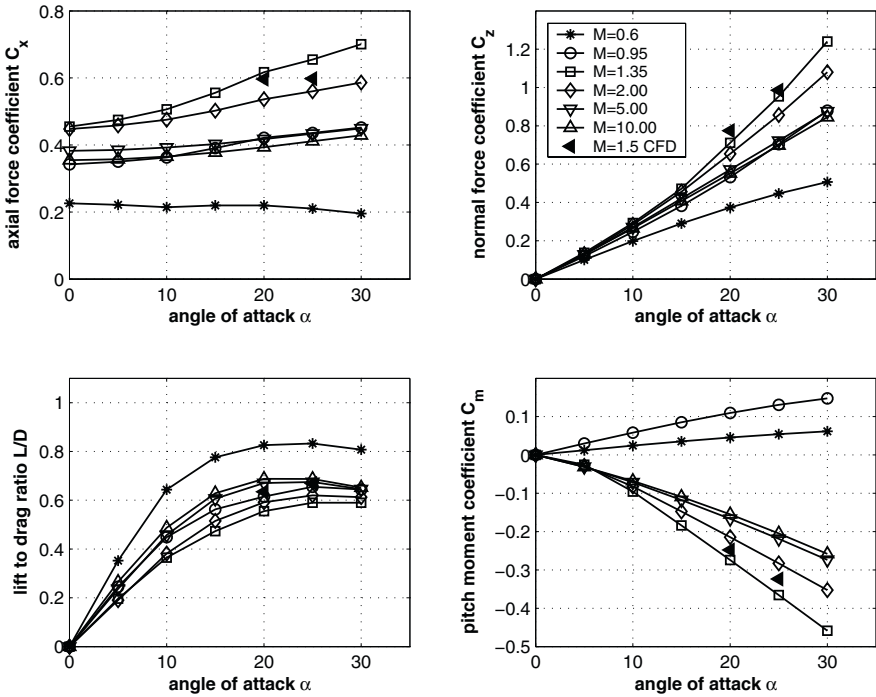


Fig. 5.22. Aerodynamic data of the bluff bicone shape, Fig. 5.8 a). Moment reference: $x_{ref} = 0.25 L_{ref}$, $z_{ref} = 0 L_{ref}$. Data source: [48].

flow by a compression shock.⁶ A further increase of L/D can be attained with a slender bicone, Fig. 5.8 b), where the reduced diameter D_1 leads to decreased axial and drag forces and a slight increase of the normal force, Fig. 5.24, [24].

The maximum L/D value for hypersonic flow amounts to 1.08. The data are assembled from wind tunnel results ($0.6 \leq M_\infty \leq 4$) and from engineering solutions ($M_\infty = 5.96$). On the other hand, the internal lay-out and the payload accommodation can be better realized with the bluff bicone (CTV) shape. As we can extract from the pitching moment graph in Fig. 5.24, for the selected moment reference point, the vehicle is unstable in the subsonic and transonic regime and only slightly stable in the supersonic and hypersonic area. Trim can only be achieved for $M_\infty = 2.53$.

The question arises on whether there exists a center-of-gravity location where, for all Mach numbers, statically stable and trimmed flight can be secured. In Fig. 5.25, the pitching moment for such a point ($x_{ref} = 0.42 L_{ref}$, $z_{ref} = -0.1467 L_{ref}$, Bicone_Tsnii shape) is plotted, but it seems rather

⁶ Since the embedded shock is formed in the flow field away from the wall, it has no clear footprint in the wall pressure distribution, Fig. 5.23 right at $X \approx 1.75$.

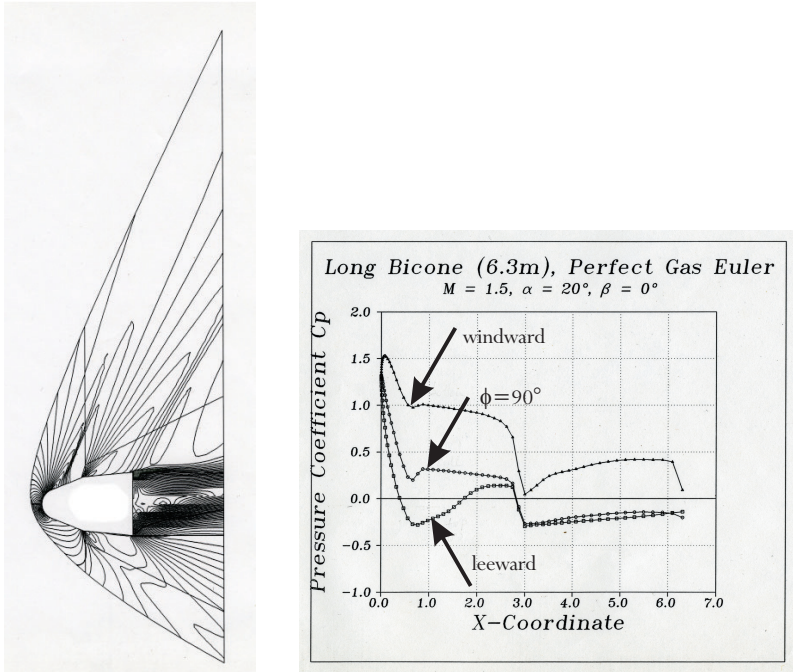


Fig. 5.23. Mach number isolines (left) and wall pressure distributions (right) in three planes of the bluff bicone shape, $M_\infty = 1.5$, $\alpha = 20^\circ$. Data source: [48].

doubtful if in practice the layout designer can realize this *cog* location. The Bicone.Dasa shape does not have such a point, which means that for Mach numbers lower than unity other arrangements have to be made.

The hypersonic flow for the bent bicone, as shown in Fig. 5.8 c), was investigated experimentally in wind tunnels ($M_\infty = 6$ and 10) [37]. Bent bicones generate an asymmetric flow field even for zero incidence which supports the trim capability of the shape, as can be seen in Fig. 5.26. Hypersonic trim is possible for realistic center-of-gravity locations and angles of attack. The figure shows, compared to that one for the symmetric bicone, an additional reduction of the axial force, in particular for low angles of attack, which lets the lift-to-drag ratio grow to a maximum of $L/D \approx 1.45$. This is still of order 1 at hypersonic trim ($22^\circ \lesssim \alpha_{trim} \lesssim 24^\circ$).

Despite the fact, that the aerodynamic performance of bicones is superior to that of classical capsules, none of these configurations were ever flown. This may have a historical background, because the aerodynamic data bases are much more complete for capsules and in addition for them real flight experience is available. Since this is not the case for bicones, the possible risks in this regard have obviously hindered any development of such systems.

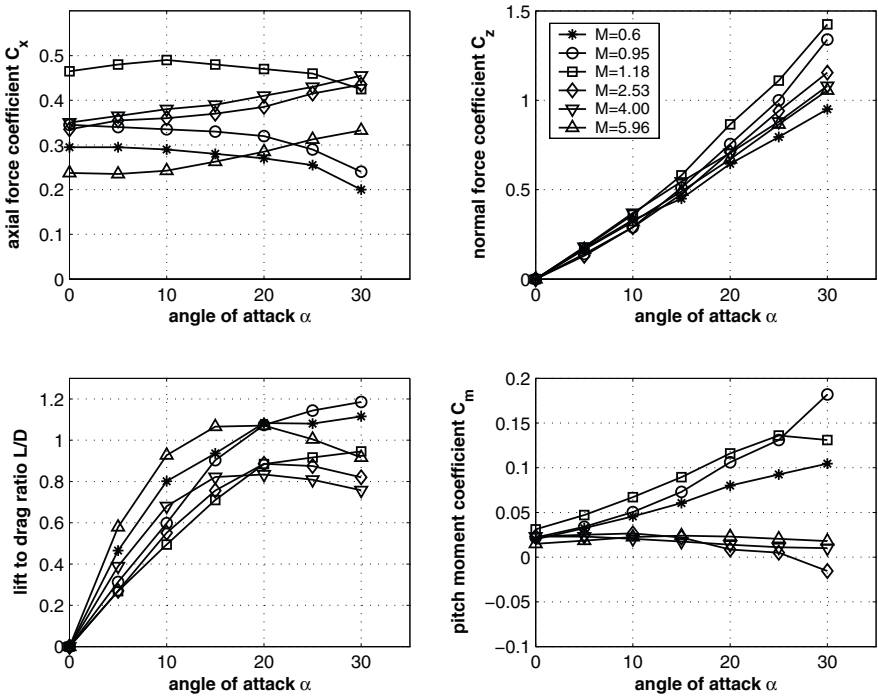


Fig. 5.24. Aerodynamic data of the slender bicone (Tsnimash) shape, Fig. 5.8 b). Moment reference: $x_{ref} = 0.57 L_{ref}$, $z_{ref} = -0.0667 L_{ref}$. Data source: [24].

5.3.7 Influence of High Temperature, Real Gas Effects on Forces and Moments

The first indications that high temperature real gas effects can have a considerable influence on the aerodynamic forces and moments at hypersonic speed were given by the APOLLO experience. There, the trim angle measured during flight was approximately 3° lower than predicted. Also, the observation during the first Space Shuttle Orbiter flight, Sections 3.5 and 3.6, that a non-predicted pitch-up moment was generated, which was due to a forward shift of the center-of-pressure, has likely the same physical cause. At that time it was argued for APOLLO that the following three physical phenomena could be responsible for that:

- compressibility (Mach number effects),
- hypersonic viscous interaction,
- high temperature real gas effects.

Today we know that the main effect is due to the thermodynamic state of the air which is strongly heated up in the hypersonic bow shock layer.

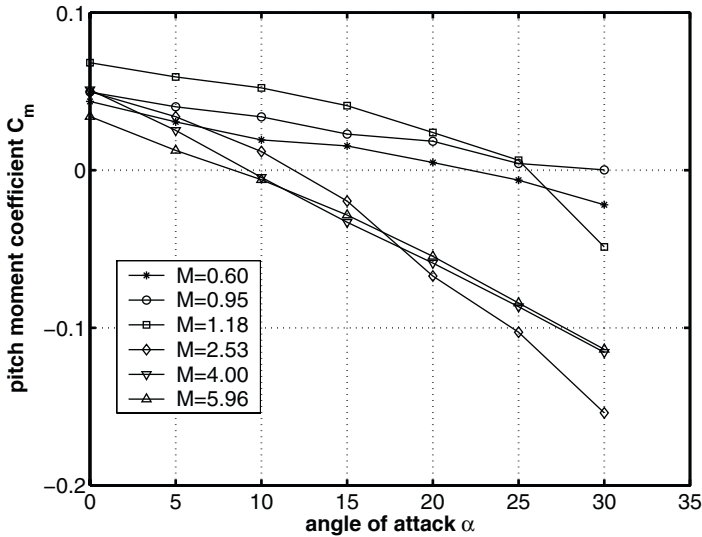


Fig. 5.25. Pitching moment for stable and trimmed flight of the slender bi-cone (Tsniimash) shape, Fig. 5.8 b). Moment reference: $x_{ref} = 0.42 L_{ref}$, $z_{ref} = -0.1467 L_{ref}$. Data source: [24].

During the APOLLO project, neither numerical nor experimental means were available for investigating possible influences of real gas effects on the aerodynamic behavior. With the advent of numerical simulation methods, solving the Euler, Navier–Stokes or the Boltzmann equation, and new high-enthalpy, ground simulation facilities, this situation has changed. In [38] a Navier–Stokes solver with an equilibrium and non-equilibrium real gas approach was applied to the front part of a two-dimensional APOLLO-like shape. This method contained besides the chemical reactions, the vibrational and electron excitations in a non-equilibrium state as well. Since non-equilibrium was assumed, the vibrational and electron excitation states were described by a second temperature T_{vibr} , which can be quite different from the rotational-translational temperature T depending on the degree of vibrational non-equilibrium.⁷ The computations showed that indeed the pitching moment of the generic APOLLO-like shape was increased due to the real gas effects, with the consequence of reduced trim angles. Further, the peak of the pressure profile along the wall was slightly shifted to the windward side which is characteristic for flows with real gases.

Since these effects are so important for reliable entry flights from space, in the European MSTP with the Atmospheric Re-entry Demonstrator ARD, strong efforts were undertaken to reveal this problem. More than 120 com-

⁷ The governing equations for this approach can be found in detail in Appendix A.

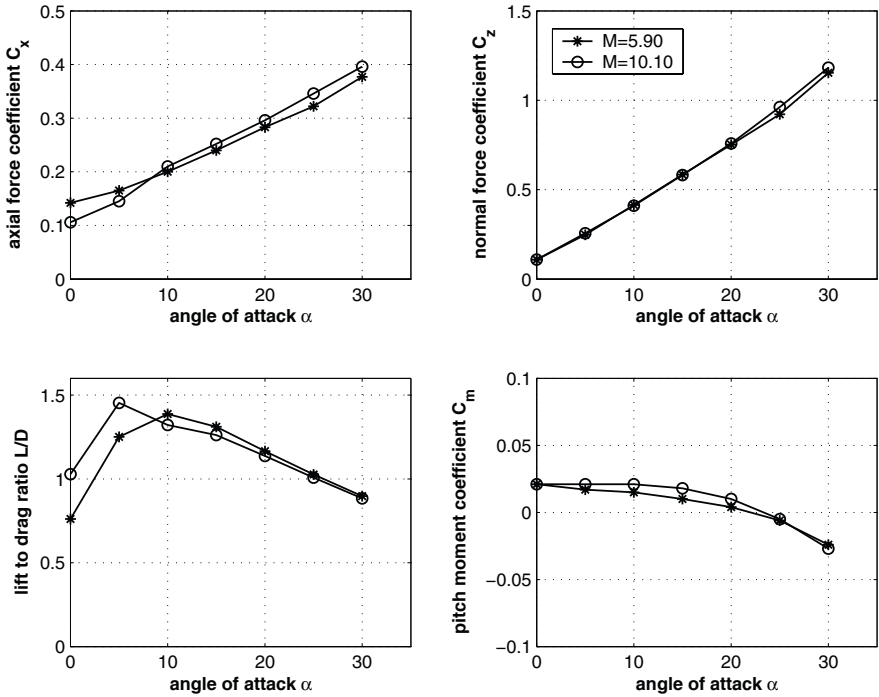


Fig. 5.26. Aerodynamic coefficients in the hypersonic regime for the bent bicone shape, Fig. 5.8 c). Moment reference: $x_{ref} = 0.554 L_{ref}$, $z_{ref} = 0 L_{ref}$. Data source: [37].

plete three-dimensional Euler and Navier–Stokes computations at predicted (pre-flight) and measured (post-flight) trajectory points were conducted with perfect, equilibrium and non-equilibrium thermochemical states of the air, [9, 51, 52]. A summary of these results is given in Fig. 5.27.

All the computations were conducted for an angle of attack $\alpha = -20^\circ$. Mach number independence is well discernible for C_X , C_Z , and L/D . However, the thermodynamic state of the gas affects considerably the aerodynamic coefficients C_X , C_Z as well as the aerodynamic performance L/D . The axial force coefficient C_X is best represented by the equilibrium assumption (upper left) and the normal force coefficient C_Z by the non-equilibrium one (upper right). The lift-to-drag ratio L/D is not much affected, but the non-equilibrium state seems to be the appropriate one (lower left).

Finally, the trim angle α_{trim} in particular for high Mach numbers, agrees fairly well with the non-equilibrium data (lower right). The trim angles are computed with Park's formula, eq. (5.7). Indeed, for high Mach numbers the differences of α_{trim} between perfect gas predictions and flight are more than 2° , which is in agreement with the observations during APOLLO flights. From

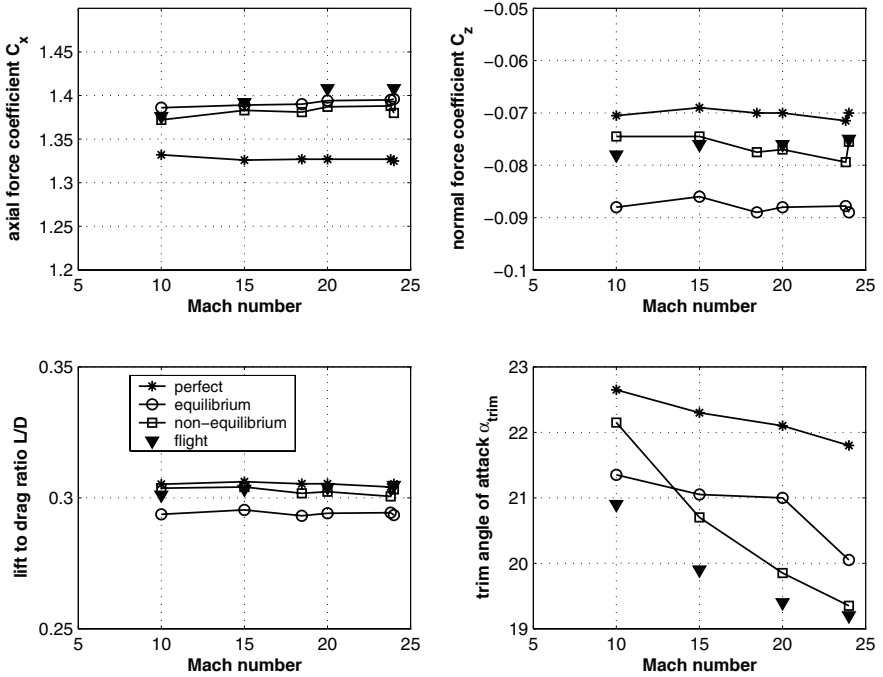


Fig. 5.27. Influence of high temperature real gas effects on the aerodynamics of the ARD capsule, angle of attack $\alpha = -20^\circ$. Data source: [9, 51, 52], center-of-gravity: $x_{cog} = 0.26 D_1$, $z_{cog} = 0.0353 D_1$.

these results it can be concluded that perfect gas simulations, either numerically or experimentally, are not appropriate for re-entry flows with high Mach numbers, say $M_\infty \gtrsim 6$.

5.4 Dynamic Stability

When a capsule or ballistic probe enters a planetary atmosphere the incidence of this vehicle evolves like an oscillator responding to the aerodynamically static and dynamic forces and moments. If the vehicle exhibits static stability, the static torque always tends to restore the vehicle towards the trim position during its oscillatory motion. If the vehicle exhibits dynamic stability, the am-

plitude of the oscillatory motion is then damped,⁸ reaching asymptotically⁹ the stable trim position.

Since the 1960s, it is well-known that capsules and ballistic probes, widely used in planetary exploration missions, often exhibit dynamic instabilities during the landing phase. This may concern flight velocities in the low supersonic, transonic and subsonic flow regime. The final landing operation, which is often supported by an appropriate parachute system, where the elements of this system (drogue chute \implies pilot chute \implies parachute, or similar) have to be extracted, mostly from a canister inside the vehicle and successfully deployed, requires a dynamically stable flight state of such a vehicle.

Because of the importance of dynamically stable flight in the different Mach number regimes, we give here a compact account of the issues of dynamic stability of NW-RV's, because in general this cannot be found in the literature. Generally, the dynamic stability is defined by [54]

$$\xi = C_D - \frac{\partial C_L}{\partial \alpha} + \left(\frac{L_{ref}}{r} \right) (C_{mq} + C_{m\dot{\alpha}}), \quad (5.8)$$

with C_D the drag coefficient, C_L the lift coefficient, $C_{mq} + C_{m\dot{\alpha}}$ the dynamic derivative of pitch motion, the so-called pitch damping coefficient, and r the radius of gyration of the vehicle around the pitch axis.

The vehicle is dynamically stable, if the dynamic stability coefficient

$$\xi < 0. \quad (5.9)$$

Condition eq. (5.9) is often used in ballistic range tests where it is assumed that the aerodynamic coefficients are constant for angle of attack variations, [53, 54]. However, our main interest consists in the determination of the dynamic derivative of pitch motion $C_{mq} + C_{m\dot{\alpha}}$. So we restrict the following discussion to the description of experimental and numerical methods regarding the damping properties of oscillatory movements of RV-NW's.

5.4.1 Physics of Dynamic Instability

From the beginning of the investigations of dynamic instability of blunt¹⁰ or very blunt¹¹ shapes, it was argued that the near wake flow plays an important role regarding any dynamically unstable behavior, [55, 56]. Further, experimental investigations revealed that also nose-induced flow separation and reattachment make the vehicle more unstable. Since no full and clear understanding of the related physical phenomena is available up to now, we list here

⁸ Long-period lightly damped oscillatory modes are called phugoid modes in aircraft flight dynamics.

⁹ Due to the flight along the trajectory with decreasing altitude and increasing density.

¹⁰ Spherical cones and bicones.

¹¹ Capsules and ballistic probes.

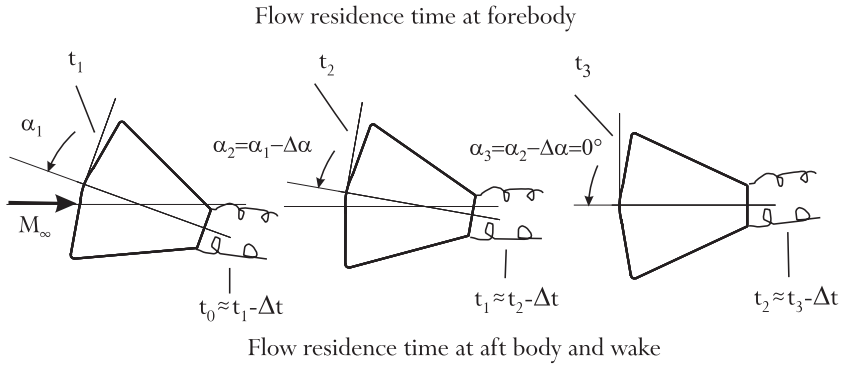


Fig. 5.28. Sketch of oscillatory pitch motion.

some experimentally observed phenomena and corresponding interpretations. Partly they are contradicting each other, which illustrates the poor present state of the art.

- The wake influences the pitch rotation. When the vehicle and with that the aft part of the configuration comes down during the pitch movement, for example to $\alpha_3 = 0^\circ$ at time t_3 , Fig. 5.28, the aft part and, of course, the wake resides in the flow field generated by the front part of the vehicle at an earlier instant with $\Delta\alpha > 0^\circ$ for the time $t_2 \approx t_3 - \Delta t$. The time lag Δt is needed to propagate the flow information from the front part to the aft part and the wake. So, a destabilizing moment is generated, compared to the steady flow field at a fixed $\alpha_3 = 0^\circ$ position, Fig. 5.28 [55].
- Experience from many test cases with flow separation is that opposite effects on dynamic and static stability often may exist. The flow separation induces an increase of the static stability and causes dynamic instability, see, for example, Fig. 5.29 [55].
- Rounded bases on spherically blunted cones make these shapes dynamically more unstable, Fig. 5.30.
- The dynamic pressure plays a role. During entry/re-entry in a planet's atmosphere there is a rapid increase of the dynamic pressure q_∞ due to the density increase. The dynamic pressure reaches a maximum when the decrease of v_∞^2 becomes stronger than the increase of ρ_∞ , see also Fig. B.2. Typically, the vehicle exhibits dynamic stability as long as q_∞ increases and gets unstable close to the maximum and beyond [53]. An often-used explanation is that the vehicle experiences a weakened static restoring moment due to the decreasing dynamic pressure [54].
- As mentioned above the vehicles are more unstable with decreasing Mach number, which is explained with the growing influence of the pressure distribution at the aft part of the vehicle for lower Mach numbers.

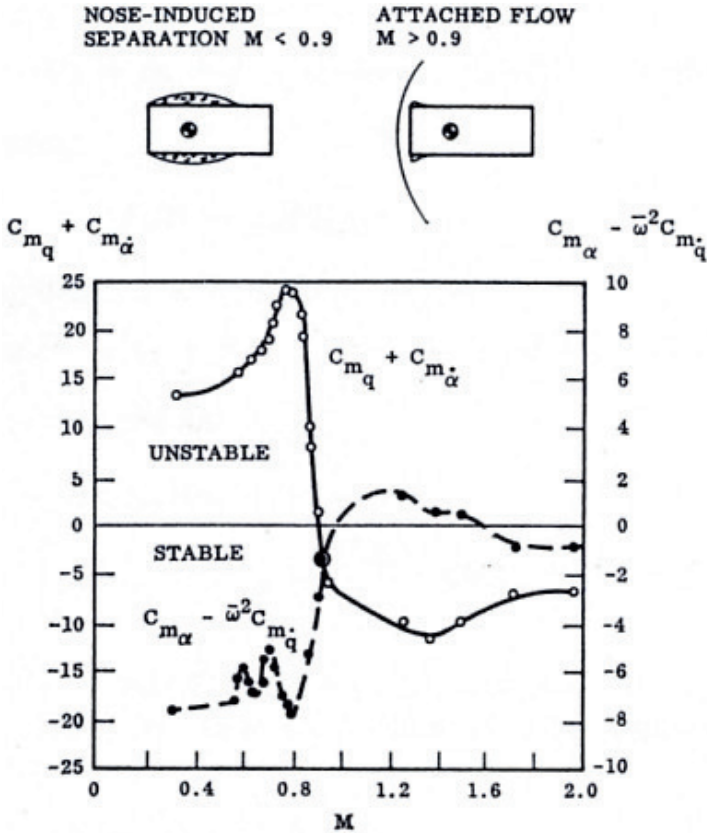


Fig. 5.29. Typical stability behavior. Flow field past a canister with separation at $\alpha_0 = 0$ and pitch angle $\Delta\theta = 1.5^\circ$ [55]. Coefficient of dynamic stability $C_{m_q} + C_{m_{\dot{\alpha}}}$ (left axis) and of static stability $C_{m_{\alpha}} - \bar{\omega}^2 C_{m_{\dot{q}}}$ (right axis, this is the notation in [55] for the static stability) as function of the lower range of the flight Mach number M .

- Hysteresis play a role [57, 58]. Analysis of the unsteady wake structure suggests that the vortical flow in the wake moves up and down with a non-dimensional frequency, defined by the Strouhal number,¹² which amounts approximately to $Sr = 0.2$. A second frequency in the flow field is associated with the free shear layer, mostly generated near the shoulder of a capsule or entry probe, where vortices are formed by the Helmholtz instability, having a Strouhal number $Sr \approx 2$. In contrast to this, the natural flight frequency of the non-winged vehicles discussed in [57], derived from the solution of the equations of angular motion, Sub-Section 5.4.2, is at least one order of mag-

¹² $Sr = fD/v_\infty$, with f the frequency, D the reference vehicle diameter and v_∞ the free-stream velocity.

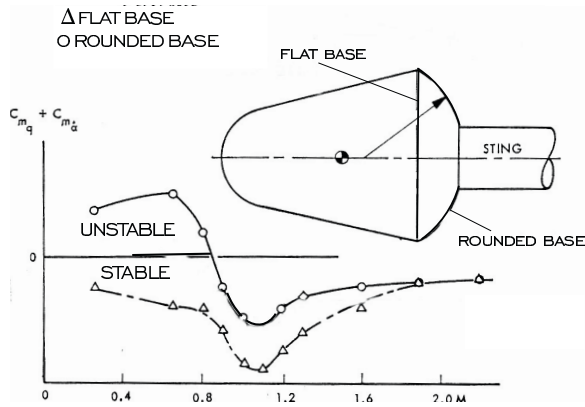


Fig. 5.30. Effect of the base contour on pitch damping at $\alpha_0 = 0^\circ$ and angular position $\Delta\theta = 1.5^\circ$ [55]. Dynamic stability coefficient $C_{m_q} + C_{m_{\dot{\alpha}}}$ as function of the flight Mach number M .

nitude lower than the aforementioned Strouhal numbers indicate. Therefore it was argued that there is no resonance coupling possible between the angular motion and the frequencies of the unsteady flow structure which induce the dynamic instability.

Instead, the pressure distribution along the vehicle’s aft part surface indicates during the oscillation a hysteresis effect, which means that at an instantaneous angular position, say at $\theta = \theta_c$, the pressure distribution during upward movement is different compared to the one during downward movement. In the case that the pitching moment C_m , evaluated by the integration of the pressure distribution around the center-of-gravity, is larger during upward compared to downward movement, an additional moment is generated which acts in the direction of the angular motion. Thus the dynamic oscillations are less damped and could become unstable. Fig. 5.31 demonstrates this behavior for a two-dimensional APOLLO-like shape.¹³

- The importance of the hysteresis effect for the dynamic stability is also described in [59]. The hysteresis effect is manifested by pressure oscillations due to the body movement at the aft part of the vehicle. A detailed analysis on the basis of reliable CFD results of flow fields with fixed angular positions¹⁴, revealed the existence of a longitudinal vortex pair generated just behind the recirculation region of the vehicle wake. From that it was conjectured that the magnitude of the lift slope $C_{L\alpha}$ plays an important role for the dynamic stability in the sense that larger $C_{L\alpha}$ values lead to a more unstable behavior.

¹³ The unstable tendency of the system is demonstrated by the direction of rotation of the moment coefficient C_m , which is clockwise in Fig. 5.31.

¹⁴ For steady free-stream conditions.

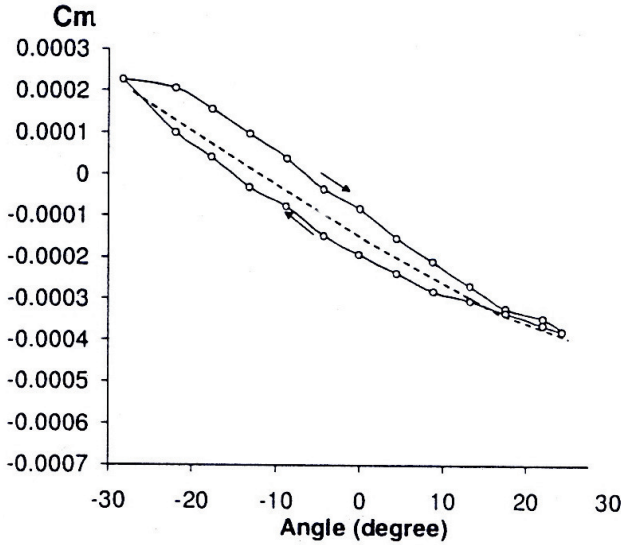


Fig. 5.31. Hysteresis due to oscillatory motion: pitching moment C_m as function of pitch angle θ [57].

5.4.2 Equation of Angular Motion

The general equation of the rate of change of angular motion reads [60]

$$T_f \left(\frac{d\Omega}{dt} \right)_g = T_f \left(\frac{d\Omega}{dt} \right)_f + \underline{\Omega}_f \times T_f \underline{\Omega}_f = \underline{Q}_f^a, \quad (5.10)$$

$$T = \begin{pmatrix} I_{xx} & -I_{xy} & -I_{zx} \\ -I_{xy} & I_{yy} & -I_{yz} \\ -I_{zx} & -I_{yz} & I_{zz} \end{pmatrix}, \quad \underline{\Omega} = \begin{pmatrix} p \\ q \\ r \end{pmatrix}, \quad \underline{Q}^a = \begin{pmatrix} L \\ M \\ N \end{pmatrix}, \quad (5.11)$$

with T being the moment of inertia tensor, $\underline{\Omega}$ the vector of angular velocity, and \underline{Q}^a the vector of aerodynamic moments. The subscript g denotes the inertial, Earth-fixed (geodetic), and f the non-inertial (vehicle fixed, i.e., body-axis) coordinate system, which are depicted in Fig. 5.32. The aerodynamic entities are specified by the superscript a ; L , M , N are the total roll, pitch and yaw moments, and p , q , r are the angular roll, pitch and yaw velocity components.

The three components of the vector-matrix equation, eq. (5.10), have the form

$$\begin{aligned} I_{xx}\dot{p} - I_{xy}\dot{q} - I_{zx}\dot{r} + q(-I_{zx}p - I_{yz}q + I_{zz}r) - r(-I_{xy}p + I_{yy}q - I_{yz}r) &= L, \\ -I_{xy}\dot{p} + I_{yy}\dot{q} - I_{yz}\dot{r} + r(I_{xx}p - I_{xy}q - I_{zx}r) - p(-I_{zx}p - I_{yz}q + I_{zz}r) &= M, \end{aligned} \quad (5.12)$$

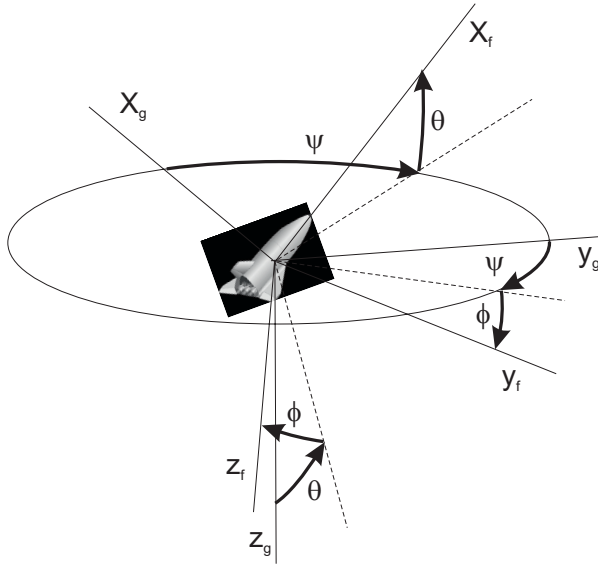


Fig. 5.32. Definition of the Euler angles (ϕ, θ, ψ) transforming geodetic (g) to vehicle fixed (f) coordinate systems.

$$-I_{zx}\dot{p} - I_{yz}\dot{q} + I_{zz}\dot{r} + p(-I_{xy}p + I_{yy}q - I_{yz}r) - q(I_{xx}p - I_{xy}q - I_{zx}r) = N.$$

For vehicles, being symmetrical in the x - z plane with $I_{xy} = I_{yz} = 0$, they reduce to

$$\begin{aligned} I_{xx}\dot{p} - I_{zx}\dot{r} + q(-I_{zx}p + I_{zz}r) - rI_{yy}q &= L, \\ I_{yy}\dot{q} + r(I_{xx}p - I_{zx}r) - p(-I_{zx}p + I_{zz}r) &= M, \\ -I_{zx}\dot{p} + I_{zz}\dot{r} + p(I_{yy}q) - q(I_{xx}p - I_{zx}r) &= N. \end{aligned} \tag{5.13}$$

The angular orientation of the vehicle in the inertial space is described by the Euler angles ψ (heading angle), θ (pitch angle) and ϕ (bank angle), Fig. 5.32:

$$\underline{\Omega}_f = \begin{pmatrix} p \\ q \\ r \end{pmatrix}_f = \begin{pmatrix} 1 & 0 & -\sin\theta \\ 0 & \cos\phi & \sin\phi \cos\theta \\ 0 & -\sin\phi & \cos\phi \cos\theta \end{pmatrix} \begin{pmatrix} \dot{\phi} \\ \dot{\theta} \\ \dot{\psi} \end{pmatrix}. \tag{5.14}$$

The components of the vector-matrix equation, eq. (5.14), in detail read

$$\begin{aligned} p &= \dot{\phi} - \dot{\psi} \sin\theta, \\ q &= \dot{\theta} \cos\phi + \dot{\psi} \sin\phi \cos\theta, \\ r &= -\dot{\theta} \sin\phi + \dot{\psi} \cos\phi \cos\theta. \end{aligned} \tag{5.15}$$

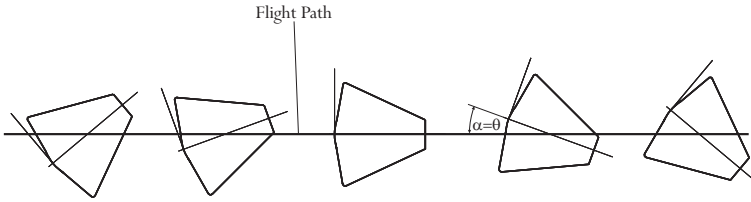


Fig. 5.33. Straight level flight of an RV-NW which oscillates in the pitch plane.

Due to the rotational symmetry of most RV-NW's, a consideration of the angular motion restricted to the x - z (pitch) plane is often sufficient (one degree of freedom of rotation) for determining the dynamic stability. Thus $\phi = \psi = p = r = 0$, and eqs. (5.13) and (5.15) reduce to

$$I_{yy} \dot{q} = I_{yy} \ddot{\theta} = M. \quad (5.16)$$

Consider now the flight of a RV-NW. For convenience we assume straight level flight, Fig. 5.33. The vehicle, after being disturbed, may oscillate in the pitch plane initially with a small angular amplitude when the disturbance is small. The question is now whether this oscillatory movement will be damped or will be amplified. In the first case, we speak about a dynamically stable vehicle; in the latter, about a dynamically unstable vehicle. For an oscillatory movement with small pitch angles $\theta(t)$ around a fixed angle of attack α , the moment M in eq. (5.16) is written as the sum of two terms:

$$M(\theta) = \frac{\partial M^a}{\partial \theta} \theta + \frac{\partial M^a}{\partial \dot{\theta}} \dot{\theta}, \quad (5.17)$$

where $\dot{\theta}$ is the rate of change with time t of pitch movement. The assumptions and conditions which are used in the derivation of eq. (5.17) are described in detail in [61].

The first term of this relation is called the aerodynamic restoring moment because for $M_\theta^a < 0$ (static stability), it yields $M \rightarrow 0$, i.e., stable flight. The second term is called the aerodynamic damping moment, because for $M_{\dot{\theta}}^a < 0$ (dynamic stability), it reduces M as a function of time t , $M(t) \rightarrow 0$, i.e., the pitch oscillation is damped with time.

The movement shown in Fig. 5.33 can be considered as the sum of two movement forms, namely a pitch oscillation with angular pitch velocity q at constant angle of attack α , and an angle of attack oscillation with constant pitch angle θ . Superimposed they result in the straight flight path shown in the figure.

In the first movement form, the vehicle moves with oscillating pitch angle θ (θ is the position of the vehicle's x -axis) and constant angle of attack along a curved flight path, Fig. 5.34. The pitching moment hence is a function of the pitch velocity $q = \dot{\theta}$, and its rate of change with q is $\partial M / \partial q = M_q$.

In the second movement form, the vehicle moves along a curved flight path with constant pitch angle, which acts on the vehicle as an angle of attack change with time, Fig. 5.35. The pitching moment hence is a function of the angle of attack velocity $\dot{\alpha}$, and its rate of change with $\dot{\alpha}$ is $\partial M/\partial \dot{\alpha} = M_{\dot{\alpha}}$.

This means that the aerodynamic damping moment can thought to be composed of two terms

$$M_{\dot{\theta}}^a = M_q^a + M_{\dot{\alpha}}^a. \tag{5.18}$$

And finally we obtain

$$M = M_{\theta}^a \theta + (M_q^a + M_{\dot{\alpha}}^a) \dot{\theta}. \tag{5.19}$$

In wind tunnel experiments (free or forced oscillation), the measured total moment M in eq. (5.17) has to be expanded by the components of the elastic restraints considered as a tare moment M^t (for more details see [61, 53])

$$M = (M_{\theta}^a + M_{\theta}^t) \dot{\theta} + (M_{\theta}^a + M_{\theta}^t) \theta. \tag{5.20}$$

In the non-dimensional form we find for the aerodynamic coefficient of pitch damping, also called dynamic derivative of pitch motion¹⁵

$$C_{mq} + C_{m\dot{\alpha}} = M_{\dot{\theta}}^a \frac{2v_{\infty}}{q_{\infty} A_{ref} D^2}. \tag{5.21}$$

If its value is negative, damping occurs, the vehicle is dynamically stable. The coefficient of the slope of the pitching moment, i.e., its derivative with respect to the angle of attack, reads

$$C_{m\alpha} = M_{\theta}^a \frac{1}{q_{\infty} A_{ref} D}. \tag{5.22}$$

If its value is negative, the vehicle is statically stable. Note that D denotes the diameter of the RV-NW. The reader is asked to note that a vehicle can be statically stable but dynamically unstable and vice versa; see, e.g., Fig. 5.29.

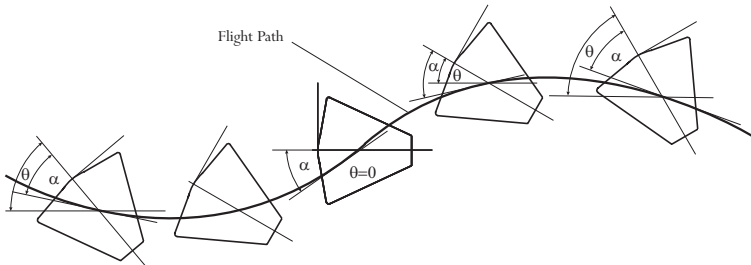


Fig. 5.34. Pitch plane: oscillation with pitch velocity q at constant angle of attack α leads to M_q .

¹⁵ $C_{mq} + C_{m\dot{\alpha}}$ is the usual notation for the dynamic derivative of pitch motion.

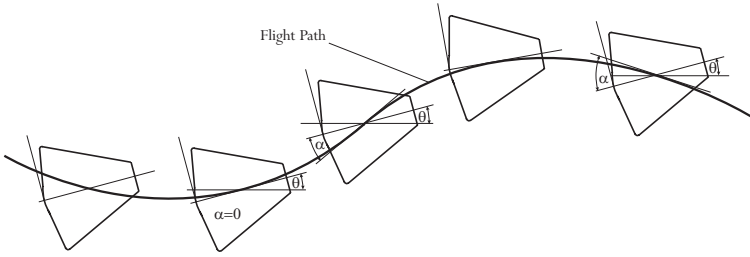


Fig. 5.35. Pitch plane: angle of attack oscillation at constant pitch angle θ leads to $M_{\dot{\alpha}}$.

5.4.3 Experimental Methods

Up to now the dynamic stability of flight vehicles is determined mainly by experimental methods [53, 61, 62]:

- free oscillation technique,
- free-to-tumble technique,
- forced oscillation technique,
- free flight technique.¹⁶

As already mentioned in Sub-Section 5.4.2, for RV-NW's, it is sufficient to determine the pitch damping coefficient $C_{mq} + C_{m\dot{\alpha}}$ for a proper assessment of the dynamic stability of the vehicle. In the following we treat briefly the capabilities of the first three techniques including the data reduction processes, which are most often used for capsule and entry probe investigations.

Free Oscillation Technique

This method is probably the earliest and obviously the simplest technique to determine the damping coefficient. The model, mounted on a sting and fixed by an elastic flexure, is deflected to an initial amplitude, then released and the decay of the oscillatory motion in the presence of flow is observed. No complicated drive or control system is required. On the other hand, this technique fails if the model is dynamically unstable, which means that the initial amplitude is amplified and no control of the angular motion is possible. Nevertheless, such behavior would indicate that the model possesses a strong dynamic instability.

For the determination of the dynamic coefficient, we consider the equation of angular motion (harmonic motion with small amplitudes) in the form of eqs. (5.16) and (5.20):

$$I_{yy}\ddot{\theta} = (M_{\theta}^a + M_{\theta}^t)\dot{\theta} + (M_{\theta}^a + M_{\theta}^t)\theta. \quad (5.23)$$

For further consideration we rewrite eq. (5.23) in the form

¹⁶ In ballistic wind tunnels.

$$I_{yy}\ddot{\theta} + C\dot{\theta} + K\theta = 0, \quad (5.24)$$

where the damping parameter C , and the restoring parameter K are:

$$C = -(M_{\dot{\theta}}^a + M_{\dot{\theta}}^t), \quad K = -(M_{\theta}^a + M_{\theta}^t). \quad (5.25)$$

The solution of eq. (5.24), which is of interest for us, represents the conditions where the system will oscillate and reads¹⁷

$$\begin{aligned} \theta &= A_1 e^{(a+bi)t} + A_2 e^{(a-bi)t} \quad \text{or} \\ \theta &= \theta_0 e^{-(C/2I_{yy})t} \sin(\omega_d t \pm \phi), \end{aligned} \quad (5.26)$$

where $a = -C/2I_{yy}$, $b = \omega_d = \sqrt{(K/I_{yy}) - (C/2I_{yy})^2}$ is the damped natural frequency, and A_1, A_2, θ_0, ϕ are arbitrary constants. The oscillatory system, eq. (5.24), is damped if $a < \omega_n$ or $-C/2I_{yy} < \sqrt{K/I_{yy}}$, where ω_n is the undamped natural frequency.

From the measured time history of the oscillatory motion the decrease of the amplitude θ as function of time is known. By definition of the logarithmic decrement at times t_1 and t_2 we obtain from eq. (5.26) (with $\sin(\omega_d t \pm \phi) = 1$)

$$\begin{aligned} \ln \frac{\theta_2}{\theta_1} &= -(C/2I_{yy})(t_2 - t_1), \\ C &= -\frac{2I_{yy}f}{C_{yr}} \ln \frac{\theta_2}{\theta_1}, \end{aligned} \quad (5.27)$$

where $t_2 - t_1 = C_{yr}/f$, C_{yr} is the number of cycles damped during $\Delta t = t_2 - t_1$ and f the frequency of oscillation.

The restoring (static) parameter is

$$K = I_{yy}\omega_d^2 + I_{yy} \left(\frac{C}{2I_{yy}} \right)^2, \quad (5.28)$$

where the second right-hand side term is usually very small and can be neglected. Therefore we have

$$K = I_{yy}\omega_d^2. \quad (5.29)$$

As mentioned in Sub-Section 5.4.2, the dynamic damping and the static restoring moment consist of the aerodynamic moments and the moments generated by tares¹⁸ in the mechanical system. The tares are given from wind-off measurements and we find [61]:

$$\begin{aligned} C &= -(M_{\dot{\theta}}^a + M_{\dot{\theta}}^t)_w, \\ K &= -(M_{\theta}^a + M_{\theta}^t)_w, \\ M_{\theta}^a &= (M_{\theta}^a + M_{\theta}^t)_w - (M_{\theta}^t)_v, \\ M_{\theta}^a &= (M_{\theta}^a + M_{\theta}^t)_w - (M_{\theta}^t)_v, \end{aligned} \quad (5.30)$$

¹⁷ The roots of the characteristic equation are complex.

¹⁸ Tare damping comprises the damping by the mechanical system, the damping capacity of the materials and the damping of still air in wind-off condition.

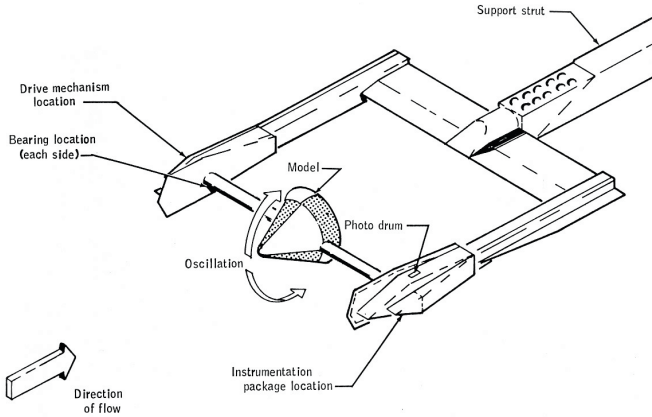


Fig. 5.36. Model installation in free-to-tumble dynamic tests [22].

where the subscripts w and v denote wind-on and vacuum conditions¹⁹, respectively. Finally we obtain:

$$M_{\theta}^a = -2I_{yy} \ln \frac{\theta_2}{\theta_1} \left[\left(\frac{f}{C_{yr}} \right)_w - \left(\frac{f}{C_{yr}} \right)_v \frac{f_v}{f_w} \right], \quad (5.31)$$

$$M_{\theta}^a = -I_{yy} [(\omega_d)_w^2 - (\omega_d)_v^2], \quad (5.32)$$

which includes a correction for the tare damping considering the different oscillation frequencies in the wind-on and wind-off case. With the relations eqs. (5.21) and (5.22) the aerodynamic pitch damping coefficient of the vehicle is known.

Free-to-Tumble Technique

Models mounted on a transverse rod through its center-of-gravity are statically balanced and are able to tumble freely through an α range from 0° to 360° , Fig. 5.36. This free-to-tumble technique was extensively employed during the APOLLO programme [19, 22, 53]. In some Mach number ranges, tare damping is negligible. For Mach numbers where tare damping is expected to be a fractional part of the total damping, corrections to the input data are applied. Consequently, in eq. (5.23) M_{θ}^t and M_{θ}^t are neglected and we have

$$I_{yy} \ddot{\theta} - \frac{q_{\infty} A_{ref} D^2}{2v_{\infty}} (C_{mq} + C_{m\dot{\alpha}}) \dot{\theta} - q_{\infty} A_{ref} D C_{m\alpha} \theta = 0. \quad (5.33)$$

¹⁹ Vacuum conditions are used in order to prevent any influence of still air damping.

In eq. (5.33), $C_{mq} + C_{m\dot{\alpha}}$ is the only unknown because I_{yy} is measured in advance and $C_{m\dot{\alpha}}$ is known from static tests. Therefore, the pitch damping coefficient is found by an iteration process, changing the value of $C_{mq} + C_{m\dot{\alpha}}$ until the measured time history coincides with the computed one.

Forced Oscillation Technique

An experimental means to quantify the dynamic instability is given by the forced oscillation technique.²⁰ The model is fixed, for example, on a crossed-flexure pivot mounted on a sting and is forced to oscillate by a special apparatus, [53, 61, 62].

The oscillation frequency should be at or near the resonant frequency of the model, since this minimizes the torque required to sustain the oscillation and simplifies the determination of the dynamic derivatives. The resonance conditions can be achieved by tuning the oscillation frequency of the forcing torque until the phase shift between the forcing torque and the model displacement amounts to $\phi = 90^\circ$. The equation of angular motion, which describes the motion of a model (which is rigidly suspended in an airstream and forced to oscillate by a sinusoidal function of time) has the form

$$I_{yy}\ddot{\theta} + C\dot{\theta} + K\theta = M \cos \omega t, \quad (5.34)$$

where C and K are defined by eq. (5.25). Here, M denotes the forcing moment and ω the oscillation frequency. A particular solution of eq. (5.34) is given by:

$$\theta = \theta_0 \cos(\omega t - \phi). \quad (5.35)$$

By substituting the angular velocity $\dot{\theta}$ and the angular acceleration $\ddot{\theta}$ in eq. (5.34) and equating coefficients we obtain

$$\theta_0 = \frac{M}{(K - I_{yy}\omega^2) \cos \phi + C\omega \sin \phi},$$

$$\tan \phi = \frac{C\omega}{K - I_{yy}\omega^2}. \quad (5.36)$$

In the case of a constant amplitude motion and resonance conditions ($\phi = 90^\circ$), the inertia term balances the restoring moment parameter K , and the damping moment parameter C is proportional to the forcing moment M

$$K = I_{yy}\omega_n^2, \quad (5.37)$$

$$C = \frac{M}{\theta_0\omega}. \quad (5.38)$$

The restoring moment parameter K and damping moment parameter C can be determined from eq. (5.37) and (5.38), if the forcing moment M , the amplitude

²⁰ And not only the damping capability as in the free oscillation technique.

θ_0 and the oscillation frequency ω are known from measurements.²¹ With eqs. (5.30) and (5.37) we find for $M_{\dot{\theta}}^a$ and M_{θ}^a :

$$M_{\dot{\theta}}^a = -\frac{1}{\omega_w} \left[\left(\frac{M}{\theta_0} \right)_w - \left(\frac{M}{\theta_0} \right)_v \right], \quad (5.39)$$

$$M_{\theta}^a = -I_{yy}(\omega_w^2 - \omega_v^2). \quad (5.40)$$

Again, with eqs. (5.21) and (5.22), the dimensionless forms of the dynamic derivative are known.

5.4.4 Numerical Methods

Since the advent of powerful three-dimensional unsteady Navier–Stokes solvers in the late 1990s, which are able also to simulate turbulent flows, initial attempts were undertaken to directly predict dynamic derivatives by numerical methods. In [59], the unsteady flow around a capsule shape was computed and the flow field was evaluated with the goal to reveal the physical phenomena responsible for the dynamic instability. Unfortunately, no direct determination of the damping derivatives was carried out, but a so called “Constant-Delay-Model” was developed, which enables one to derive the dynamic stability parameters from flow calculations at fixed angles of attack.

With the procedure reported in [63, 64], a forced oscillation scenario was simulated by numerical methods. The vehicle experiences, for example, an oscillatory pitch rotation $\theta(t) = \theta_0 \sin \omega t$ around a fixed angle of attack α_{fix} with a reduced frequency $k = \omega_n D / v_{\infty}$. The natural undamped angular velocity ω_n is determined by eqs. (5.37) and (5.22)

$$\omega_n = \sqrt{\frac{C_{m\alpha} q A_{ref} D}{I_{yy}}}. \quad (5.41)$$

With a linear approach for the pitching moment, namely

$$C_m(t) = C_m(\alpha_{fix}) + C_{m\alpha} \theta(t) + (C_{mq} + C_{m\dot{\alpha}}) \dot{\theta}(t) \frac{D}{v_{\infty}}, \quad (5.42)$$

the dynamic damping term $C_{mq} + C_{m\dot{\alpha}}$ can be calculated by a numerical averaging process, since $C_m(t)$, $C_m(\alpha_{fix})$ and $C_{m\alpha}$ are known from the numerical solutions. Calculations performed for the X-24 and X-38 lifting vehicles show promising results and it seems that this approach has a great potential for future applications [63, 64].

²¹ For forced oscillation systems which operate off resonance the derivation of the equations of dynamic stability can be found in [61].

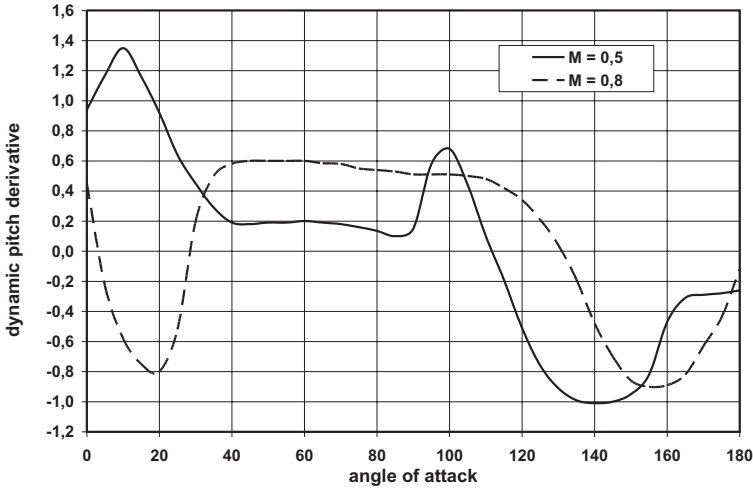


Fig. 5.37. Dynamic derivative of pitch motion $C_{mq} + C_{m\dot{\alpha}}$ as a function of the angle of attack for $M_\infty = 0.5$ and 0.8 . APOLLO shape, Fig. 5.5. Data source: [22].

5.4.5 Typical Experimental Results

There are two capsules in the world which were flown more often than any other ones. The first is the U.S. APOLLO and the second is the Russian SOYUZ, which is still in operation.²² The dynamic stability of APOLLO was investigated with the three experimental techniques which were described in Sub-Section 5.4.3.

As an example for the subsonic Mach numbers $M_\infty = 0.5$ and 0.8 , Fig. 5.37 shows the dynamic pitch derivative $C_{mq} + C_{m\dot{\alpha}}$ over an angle of attack range of $0^\circ \leq \alpha \leq 180^\circ$. In this case, the free-to-tumble test technique was applied. With the trim angles for these Mach numbers being in the range of $\alpha_{trim} \approx 15^\circ$, the vehicle exhibits dynamic stability at $M_\infty = 0.8$ but was dynamically unstable at $M_\infty = 0.5$ [22].

The SOYUZ capsule has a strong dependence of the dynamic stability on the angle of attack at $M_\infty = 0.9$, Fig. 5.38.²³ The data were obtained from wind tunnel experiments and verified in several free flight campaigns [24]. Since the trim angle α_{trim} is likely of order 20° , SOYUZ exhibits dynamic instability for that Mach number. For hypersonic Mach numbers, the capsule is stable and has only a weak dependence on α .

Chapman and Yates [54] investigated the influence of nonlinear aerodynamics during the data reduction process (both for experimental and numer-

²² SOYUZ acts as crew transporter for the ISS.

²³ In the Russian literature the notation $m_z^{\omega_z}$ is used to describe the dynamic derivative with $m_z^{\omega_z} \sim C_{mq} + C_{m\dot{\alpha}}$.

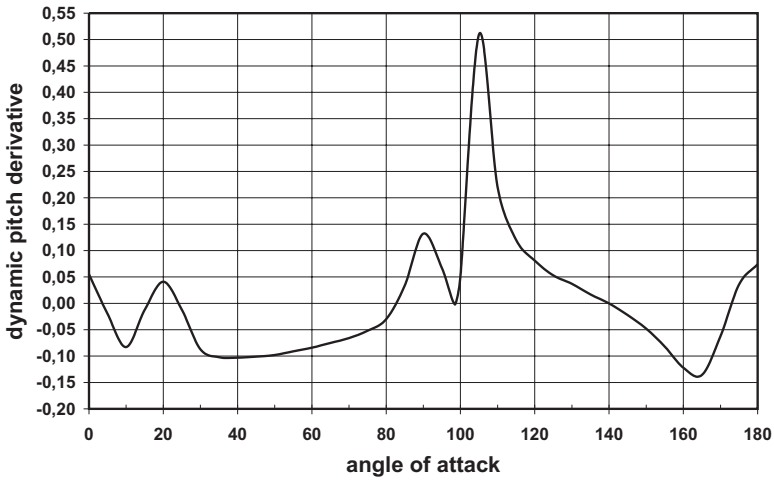


Fig. 5.38. Dynamic derivative of pitch motion $m_{z\dot{z}}$ as function of the angle of attack for $M_\infty = 0.9$. SOYUZ shape, Fig. 5.6. Data source: [24].

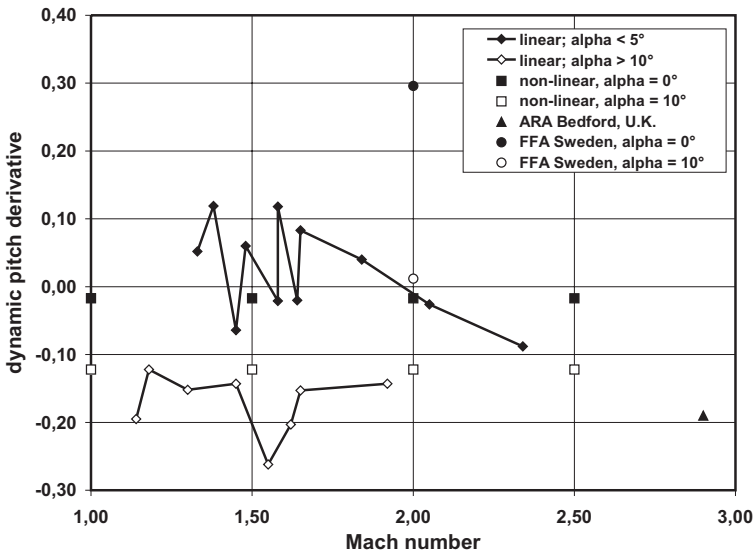


Fig. 5.39. Dynamic derivative of pitch motion $C_{mq} + C_{m\dot{\alpha}}$ as function of the Mach number. HUYGENS shape, Fig. 5.3. Data source: [53, 54].

ical data) for determining the dynamic pitch derivative $C_{mq} + C_{m\dot{\alpha}}$. For the HUYGENS Titan entry probe, the results are plotted in Fig. 5.39.

The values obtained with linear aerodynamics show a strong scatter with Mach number and support the impression of dynamic instability for the $\alpha < 5^\circ$ range. The values calculated with nonlinear aerodynamics are nearly constant ($\alpha = 0^\circ, 10^\circ$) and also exhibit a slight damping capability at $\alpha = 0^\circ$. Further, Fig. 5.39 shows two datasets of a forced oscillation experiment ($M_\infty = 2$) made at FFA, Sweden, and one dataset of a free oscillation experiment ($M_\infty = 2.9$) done by the Aircraft Research Association (ARA) in the U.K. These data were extracted from [53]. The two FFA data are not in line with the general trend and it is argued in [53] that the discrepancy is due to some open questions during the execution of the experiment. The variation of the dynamic derivative with angle of attack for supersonic Mach numbers ($M_\infty = 1.8$ and 2) is displayed in Fig. 5.40. Both curves follow the well-known trend that the dynamic stability increases with increasing angle of attack. The distribution established with the nonlinear evaluation procedure starts at $\alpha = 0^\circ$ with a small damping value, while the FFA data indicate an undamped behavior (amplification) there.

In the 1970s, the Mars entry probe VIKING for exploring the Martian atmosphere was developed in the USA. Two of these probes entered the Martian atmosphere in 1976. At that time, there were a lot of investigations regarding the dynamic stability of these entry probes [56, 53]. Since the VIKING shape is also a classical one, we present here the dynamic stability behavior, extracted

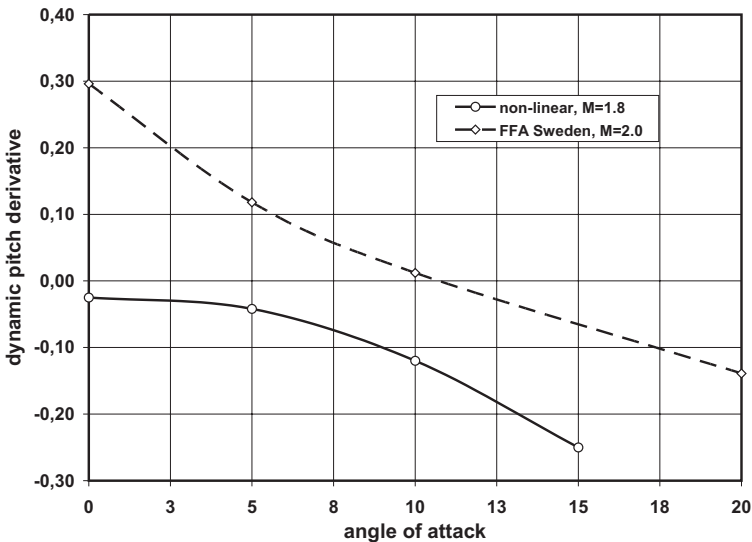


Fig. 5.40. Dynamic derivative of pitch motion $C_{mq} + C_{m\dot{\alpha}}$ as function of angle of attack. HUYGENS shape, Fig. 5.3. Data source: [53, 54].

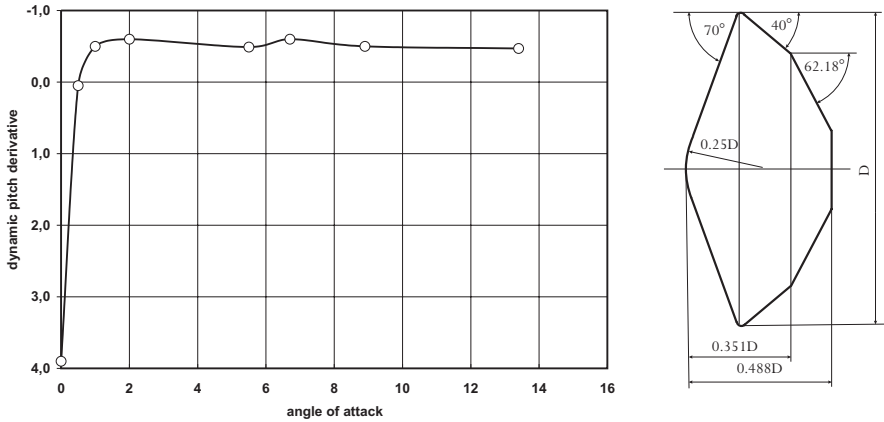


Fig. 5.41. Dynamic derivative of pitch motion $C_{mq} + C_{m\dot{\alpha}}$ as function of angle of attack, VIKING-type shape. Data source: [56].

from a free-oscillation experiment, for a typical flow case, namely, Mach number $M_\infty = 1.76$, the reduced frequency $k = 0.0069$ and the Reynolds number $Re = 7.5 \cdot 10^5$. Figure 5.41 shows the results taken from [56]. A strong instability in a small range around zero angle of attack ($\alpha < 1^\circ$) can be observed, which vanishes exponentially, leading subsequently to a positive and nearly constant dynamic damping.

In conclusion it seems that today, the uncertainties and discrepancies in the dynamic derivative data of non-winged vehicles are still large and that more activities are necessary for amending the physical understanding. Further, the test methods and the data reduction methods, which are used also for the numerical predictions, must be improved.

5.5 Thermal Loads

One of the major concerns during the development of hypersonic vehicles is the reliable prediction of the thermal loads on the airframe. These govern the design of the thermal protection system (TPS), which is one of the main contributors to the vehicle mass. The TPS mass strongly affects the magnitude of the payload mass, which is often the main issue for an efficient space mission. Generally, the peak wall temperature during re-entry defines the type of TPS material used, whereas the time-integrated heat flux governs the structure and thickness of the TPS.

During hypersonic flight, heat is transported towards the vehicle surface by three physical transport processes, Fig. 9.2, Section 9.1 [65]. The first is heat transported by diffusion in the gas towards the wall, more precisely, the heat

flux in the gas at the wall.²⁴ The second is non-convex radiation from other surface parts of the vehicle. For RV-NW's, this usually does not play a role. Thermal gas radiation of the vibrational excited, dissociated and ionized gas is the third one. For classical, low Earth orbit (LEO) re-entry with entry speeds below approximately 8 km/s, diffusive heat transfer q_{gw} is the dominating effect. On the other hand, for example, for Lunar return with an entry speed of approximately 10.6 km/s, heat transfer due to thermal gas radiation $q_{rad,g}$ becomes very important and approaches values of 50 per cent of the total heat flux. This is because of the large increase of ionized particles which are generated during entry that pass through the gas in the bow shock layer. Heat is transported away from the vehicle surface mainly by radiation cooling, but also by conduction into the structure, Section 9.1. Other cooling processes include ablation, transpiration, etc.

In Chapter 9 we give a summary of the thermal state of a vehicle surface and also, in a simulation compendium, an overview of all kinds of methods for the determination of thermal loads. In Chapter 10 relations for an approximate determination of thermal loads are provided. These are useful for first guesses and, for instance, for trajectory definition purposes. We refer the reader to Chapters 9 and 10 for details and focus our discussion now on data from three free-flight events and one technology study, namely

- OREX suborbital flight,
- ARD suborbital flight,
- APOLLO low Earth orbit (LEO) and Lunar return,
- VIKING-type shape technology study.

5.5.1 OREX Suborbital Flight

During the development and flights of APOLLO, no numerical methods with adequate quality for complete 3-D flow field simulations at corresponding trajectory points were available. Pre-flight predictions and post-flight comparisons were done with analytical relations mainly developed for predicting the forward stagnation point heating. In the 1990s, the situation changed. The data received by demonstrator flights of the Japanese OREX probe (1994) and the European ARD capsule (1998) were used to verify results of pre-flight numerical simulations and to formulate conditions for post-flight analysis including the comparison of the results obtained.

The OREX free-flight experiment gives the possibility to study how intensive is the influence of physical phenomena along the re-entry trajectory on the wall heat flux [65]. In [8, 10], viscous shock layer (VSL) and Navier–Stokes (NS) solutions were generated for selected trajectory points with various degrees of

²⁴ In the literature this is often called convective heating.

modelization, where at the wall, a temperature distribution was prescribed.²⁵ In particular, from [8], we can learn in what regime the surface catalytic behavior, the slip conditions, the thermal non-equilibrium and the number of species in the chemical model are important. The outcome was, that in the altitude regime $105\text{km} \gtrsim H \gtrsim 84\text{km}$, slip conditions and thermal non-equilibrium must be included in the NS or VSL solutions. This provides the best results for the stagnation point heating, Fig. 5.42. The wall catalycity does not play any particular role at that altitude, since the recombination probabilities are very low. For lower altitudes the influence of thermal non-equilibrium and slip conditions decreases and the wall catalycity becomes more important. The comparison with the OREX stagnation point free-flight data supports unambiguously this trend, Fig. 5.42.

In Fig. 5.43, the wall heat flux, q_{gw} over the OREX surface is plotted for an altitude of $H = 92.8$ km. Again, no differences between the calculation with non-catalytic (not shown) and finite-rate catalysis are present. The results with fully catalytic assumptions are far from being realistic. Further, the general trend is that for these altitudes the computations with slip conditions give the more realistic answer. Finally, the authors of [8] showed that the dependency on the number of species of the chemical model on the heat-flux is rather low, therefore they preferred a seven species model [65].

5.5.2 ARD Suborbital Flight

As mentioned before, another demonstration flight was conducted by the Atmospheric Re-entry Demonstrator (ARD). For the heat-flux investigations, this vehicle was subdivided into three parts, namely, the front, the rear cone and the back cover part, Fig. 5.5. The magnitude of the heat fluxes on the rear cone and back cover part is rather low compared to that on the front part, and the maximum value does not exceed 37 kW/m^2 . Nevertheless, for the proper design and sizing of the TPS system it is important to know also in this area the behavior of the flow during the flight along the trajectory. It was expected that a turbulent reattachment of the flow on the rear cone with the corresponding strong increase of the heat transfer could happen, but this was not observed. Instead, on the back cover a laminar-turbulent flow transition was detected, with a moderate increase of the heat flux [66].

But let us focus our attention on the front part. Free-flight data are available for wall-temperatures up to $\approx 1,100$ K since beyond this value the sensors did not work properly. Depending on the location of the sensors, the measured free-flight data are spread over a Mach number range of $15 \lesssim M_\infty \lesssim 26$ (corresponding to $51 \text{ km} \lesssim H \lesssim 77 \text{ km}$). The numerical simulations were carried out for $6 \lesssim M_\infty \lesssim 26$. Since in the thermo-chemical non-equilibrium flow

²⁵ The wall temperature distribution was determined by a fluid-structure coupling process, where the radiation equilibrium state (radiation-adiabatic wall) was iteratively reached [10].

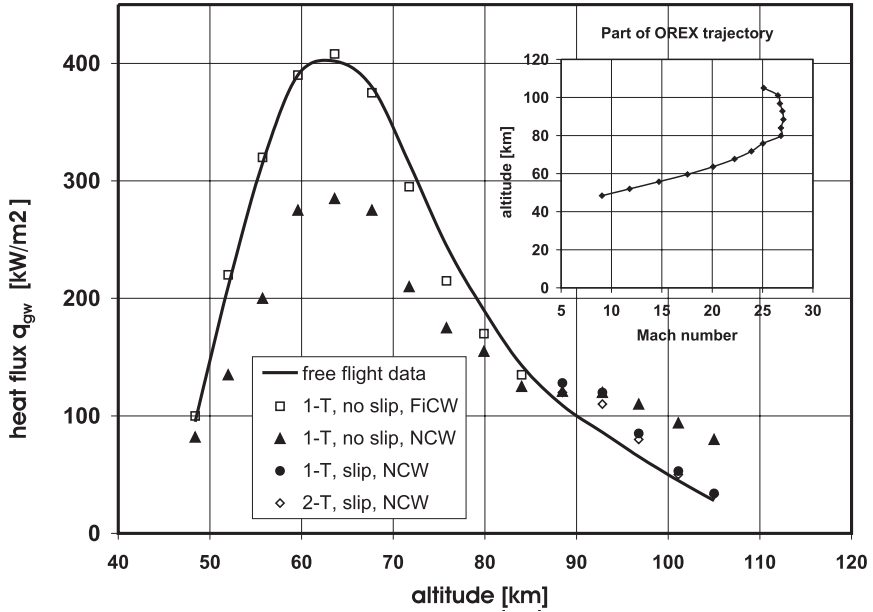


Fig. 5.42. Heat flux in the gas at the wall, q_{gw} , at the stagnation point of the OREX probe during re-entry as function of the flight altitude. Free-flight data and CFD analysis (viscous shock-layer solutions). FiCW: finite catalytic wall, NCW: non-catalytic wall, 1-T: one-temperature model, 2-T two-temperature model. Data source: [8].

regime the wall catalycity can play a major role at the same trajectory points, computations with non-catalytic and fully catalytic walls were conducted. The wall temperature distribution was calculated with the radiation-adiabatic wall condition [51, 66].

Let us first identify what is in agreement with the experience from OREX. It is the fact that for high altitudes $H \gtrsim 80$ km, the wall catalycity does not play any role and that the computations with fully catalytic wall assumption give excessively high values there (flight time $< 4,900$ s in Fig. 5.44). In the regime of the peak heating ($H \approx 64.5$ km, flight time $\approx 4,950$ s) fully catalytic NS computations provide lower values than the measured ones and even the data received from computations with chemical equilibrium are lower, which is in contradiction to the OREX results, Fig. 5.43. An explanation is, that this dispersion could be due to the pyrolysis effect of the front shield ablator, which probably affects the wall catalycity. The process itself is unknown.

On the windward side in flight, no clear transition from the laminar to the turbulent boundary layer state could be detected, but on the leeward side (near the shoulder) at an altitude $H \approx 55$ km, transition was observed [66]. The maximum heat flux was reached near the windward side shoulder, Fig. 5.45, with

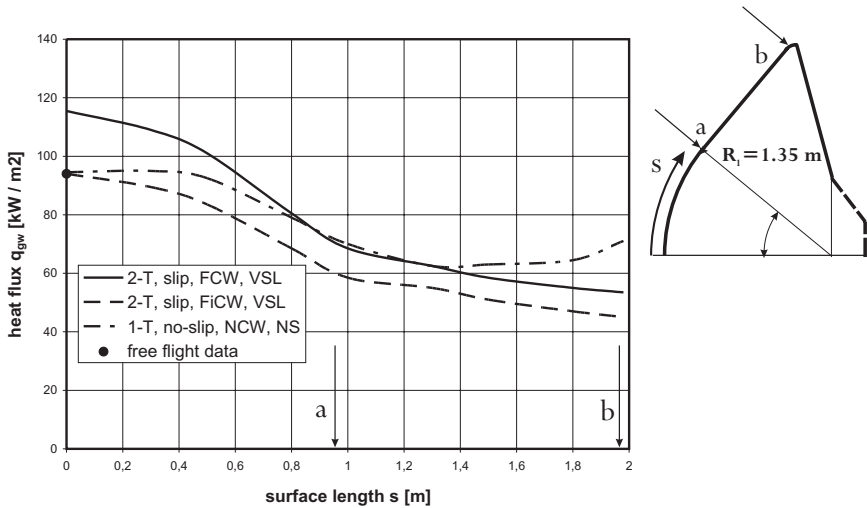


Fig. 5.43. Heat flux in the gas at the wall, q_{gw} , at the OREX probe (symmetry plane) at $v_\infty = 7,454.1$ m/s, $H = 92.8$ km, as function of the surface length s (definition in the inset). CFD analysis from viscous shock layer and Navier–Stokes solutions. FCW: fully catalytic wall, FiCW: finite catalytic wall, NCW: non-catalytic wall, 1-T: one-temperature model, 2-T two-temperature model. Free flight measurements were made only at the stagnation point ($s = 0$ m). Data source: [8, 10].

approximately $1,200$ kW/m² and the NS solutions for laminar flow with equilibrium thermodynamics are closest to the measured data. Note that in Figs. 5.44 and 5.45, the data are interpolated between the NS solutions calculated for selected trajectory points.

5.5.3 APOLLO Low Earth Orbit (LEO) and Lunar Return

A broad database exists for the APOLLO vehicle, not only from free-flight but also from wind tunnel experiments. Several attempts were made over time to duplicate these data by applying improved numerical simulation methods and physical modelling. We have learned from the discussion above (OREX and ARD flights) that for high altitudes ($H \gtrsim 80$ km), wall catalysis does not play a role on the heat flux. With decreasing altitude, catalytic effects become more and more important. The work done in [30] supports this observation, Fig. 5.46.

In [30], the heat fluxes in the pitch plane of APOLLO (x – z plane, Fig. 5.5, 2-D approach) for a Lunar aerocapturing return are calculated by different methods, ranging from simple analytical relations, Chapter 10, up to combined Euler/boundary layer solutions including non-equilibrium real gas effects. The flight conditions are: $H = 66.7$ km, $M_\infty = 32.6$, $\alpha = -20^\circ$, $v_\infty = 9,980$ m/s.

The results obtained with the latter method, and shown in Fig. 5.46, exhibit a much higher heat-flux distribution for the fully catalytic wall, with a peak value of approximately $2,000 \text{ kW/m}^2$, than with the finite rate catalytic model with peak heating of approximately $1,080 \text{ kW/m}^2$. From general experience, we conclude that the data obtained by the fully catalytic wall condition are much too high and that the data of the finite-rate catalytic model are more realistic, but further verification is necessary.

Finally, Fig. 5.47 contains from the same work the data from APOLLO wind tunnel tests. The figure shows the results of Lees' eqs. (10.71) to (10.73), and an Euler/boundary layer approach (where the boundary layer equations are solved by an integral method). The wind tunnel conditions are $M_\infty = 10.17$, $\alpha = 33^\circ$, $v_\infty = 1,440 \text{ m/s}$. Lees' method gives a much too high peak value, whereas away from $s/R = 1$, agreement with the wind tunnel data is satisfactory. Closer to the wind tunnel data are the results of the Euler/boundary layer approach, where for the peak heating also an overshoot can be observed, which, however, is considerably smaller than the one obtained with Lees formula. Nevertheless, we learn that in the early stage of a system study the application of such a simple approach like the one of Lees (but have in mind the peak heating overshoot!) can be helpful in getting a first idea of the thermal loads.

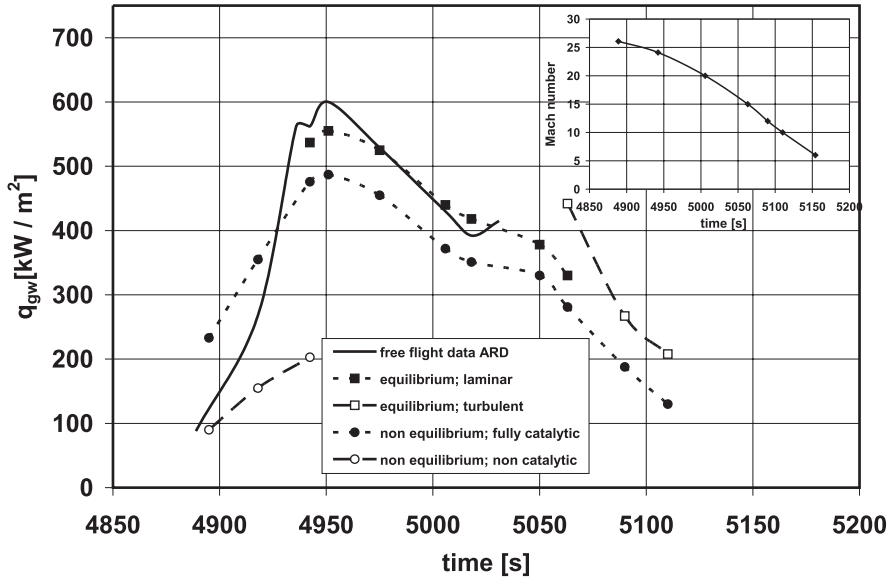


Fig. 5.44. Heat flux in the gas at the wall q_{gw} at the stagnation point of the ARD demonstrator along a part of the re-entry trajectory as function of the flight time. Free-flight data and Navier–Stokes data with different models, angle of attack $\alpha = -20^\circ$. Data source: [23, 66].

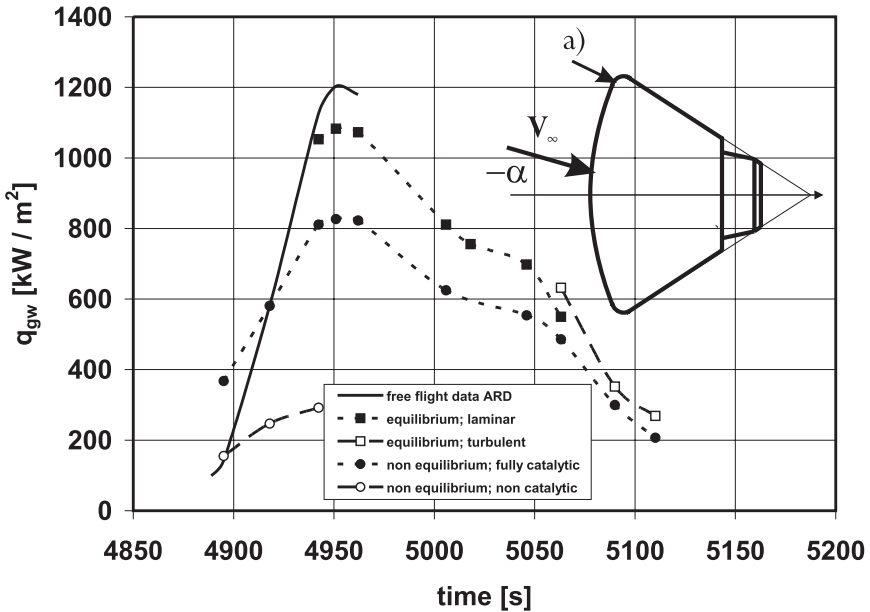


Fig. 5.45. Heat flux in the gas at the wall, q_{gw} , in point a) (peak heating regime) of the ARD demonstrator (symmetry plane) along part of the re-entry trajectory as function of the flight time (see Fig. 5.44). Free-flight data and Navier–Stokes data with different modelings, angle of attack $\alpha = -20^\circ$. Data source: [23, 66].

5.5.4 VIKING-Type Shape Technology Study

The flow field on the leeward side of either RV-W or RV-NW's moving at high Mach numbers and considerably large angles of attack contains, in general, vortical-type structures due to complex separation and reattachment/attachment processes of the flow. In this context it is important to differentiate between attachment and reattachment lines. At reattachment lines, the incoming flow in general is boundary layer material which has lost total enthalpy, for instance, due to surface radiation cooling. At attachment lines, the incoming flow in general is the outer flow²⁶ with the original total enthalpy, which may further enhance thermal loads. Depending on the topology of the velocity field at the lee side of a flight vehicle, both attachment and reattachment lines may be present [65].

The general phenomenon is called vortex/boundary layer interaction which includes also secondary and higher-order vortex-driven flow separation and reattachment phenomena. Boundary layers are becoming thick, where separation occurs (convergence of skin-friction lines) and thin in case of attachment and reattachment (divergence of skin-friction lines) [65]. In the latter case, with

²⁶ See in this respect Fig. 4.63 and the general discussion in [65].

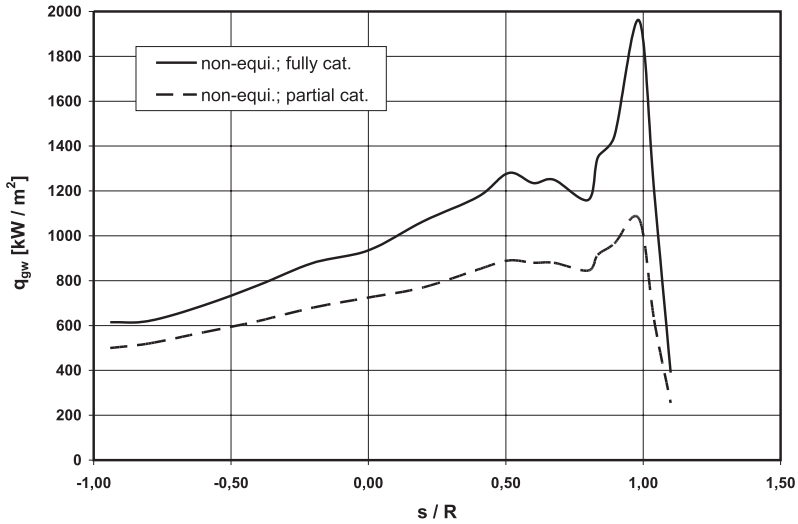


Fig. 5.46. Heat flux in the gas at the wall, q_{gw} , at the APOLLO front-shield surface (symmetry plane) as function of s/R ($s/R = 0$: center point ($z = 0$), Fig. 5.5, $s/R = 1$: stagnation point at the forward pointing shoulder). Aerocapturing Lunar return, $M_\infty = 32.6$, $H = 66.7$ km, $\alpha = -20^\circ$. Comparison of fully and partial catalytic wall conditions. Non-equilibrium Euler/boundary layer solution. Data source: [30].

the attenuation of the boundary layer, the gradients of the flow variables normal to the wall grow considerably. For gases with relatively high-enthalpy this is also valid for the gas temperature with the consequence of locally high heat fluxes in the gas at the wall q_{gw} and large wall temperatures (hot-spot situation). At separation lines, a cold-spot situation ensues.

As an example, let us consider the flow over the rear part of the VIKING 1 shape, Fig. 5.6 [45] for the moderate Mach numbers $M_\infty = 3$ at $H = 35$ km altitude, and $M_\infty = 5$ at $H = 41$ km. The angle of attack in both cases is $\alpha = -25^\circ$. We discuss a solution of the full Navier–Stokes equations [67], see also Appendix A, for turbulent flow²⁷ with a radiation-adiabatic wall boundary condition.

In Fig. 5.48 we show the attitude of the flight vehicle for the $M_\infty = 3$ case. We have noted in Sub-Section 5.2.2 that in order to achieve, for a classical axisymmetric RV-NW, a $L/D > 0$, it is necessary that the vehicle is flying with a negative angle of attack. In our case, due to the particular shape of VIKING 1, at the considered (negative) angle of attack the flow at the lower back side of the vehicle is undergoing massive separation. This is indicated by the very rugged iso-Mach lines in the figure (symmetry plane).

²⁷ A two-equation turbulence model is employed [67, 68], see also Appendix A.

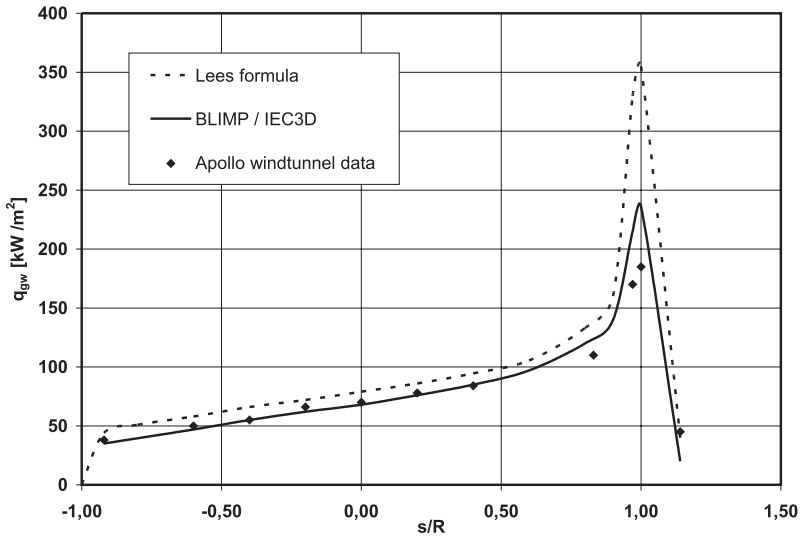


Fig. 5.47. Heat flux in the gas at the wall q_{gw} at the APOLLO front-shield surface (symmetry plane) as function of s/R (for convention see Fig. 5.46). Comparison of different prediction methods and wind tunnel data, $M_\infty = 10.17$, $\alpha = -33^\circ$. BLIMP/IEC3D: Euler/boundary layer integral method. Data source: [30].

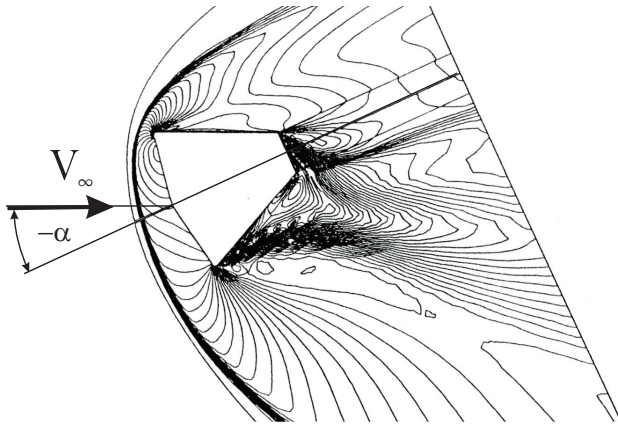


Fig. 5.48. Attitude of the VIKING 1 shape and iso-Mach lines in the symmetry plane; $M_\infty = 3$, $H = 35$ km, $\alpha = -25^\circ$ [45].

The separation pattern is expressed by the topology of the skin-friction lines on the vehicle surface.²⁸ We look first at the $M_\infty = 3$ case, Fig. 5.49. In part a) of the figure, the front view, we see that all skin-friction lines are originating in the forward stagnation point. The pattern of course is left-right symmetrical. The skin-friction lines lead over the heat shield and the shoulder to the back part and there turn downward. Immediately behind the shoulder, nearly halfway down, a convergence of skin-friction lines is discernible. It indicates squeeze-off separation [69]. Of the two involved boundary layers one comes over the shoulder from the front part of the vehicle, the other from the back part (part b) of the figure in the neighborhood of point of ‘A’).

In part b) of Fig. 5.49, we see a very particular skin-friction line pattern on the lower side of the vehicle. We do not attempt to reconstruct the complete skin-friction line topology, because the available information is not sufficient. Since we cannot decide whether we have attachment or reattachment lines, we simply speak about attachment lines. On the upper left, coming from above, we see the separation line, which we saw already in part a) of the figure. The largest part of the lower surface then is characterized by skin-friction lines running from the back towards the front part of the vehicle.²⁹

We wish to identify possible attachment/reattachment and separation lines. Therefore we consider first singular points in the skin-friction line pattern, however we note only those marked with a number. The singular point ‘1’ lies on the lower symmetry line of the body. Going upward from it, we find the points ‘2’ to ‘4.’ On the right-hand side of these points, the flow runs toward the back of the vehicle. On the left-hand side, as already observed, the flow runs towards the front part. The diverging pattern of the flow coming from ‘1’ shows that we observe here an attachment line extending to the front part. In ‘2’ it is a separation line, again an attachment line in ‘3’ and finally a separation line in ‘4.’ This holds, even if the patterns are partly tapering out.

In the $M_\infty = 5$ case, Fig. 5.50, although with lesser information available than for the $M_\infty = 3$ case, we see a much simpler skin-friction line pattern on the lower side of the vehicle. Again the largest part of the lower surface is characterized by skin-friction lines running from the back towards the front part of the vehicle. However, besides the attachment line on the lower symmetry line, now only one separation line is indicated, which ends in the singular point ‘1’ in a vortex filament, which leaves the body surface. A second separation line is discernible, which originates behind the lower shoulder of the heat shield, and runs also towards ‘1’. All this again is present left-right symmetrical on the body surface. We note that for the larger Mach number cases in [45] similarly simple skin-friction line topologies are computed. Whether in general such topologies become simpler with increasing Mach numbers is not clear.

²⁸ In general it is not possible to deduce from this surface topology fully and unambiguously the vortex and vortex sheet pattern above the surface.

²⁹ The numerical solution resulted in a steady flow field. This does not rule out the possibility that in reality this is only a time-averaged picture of a fluctuating flow field. Nevertheless, we assume steady flow throughout.

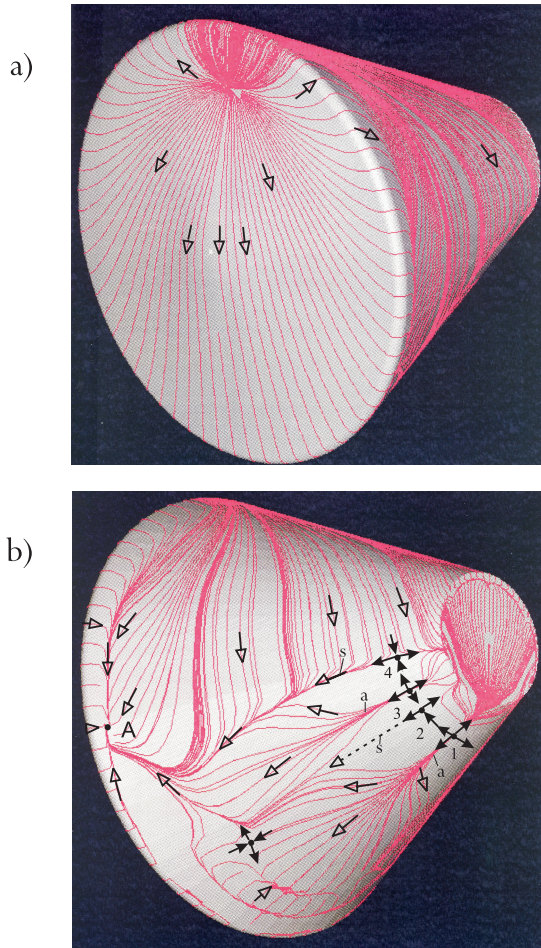


Fig. 5.49. Pattern of kin-friction lines on the surface of the VIKING 1 shape. $M_\infty = 3$, $H = 35$ km, $\alpha = -25^\circ$ [45]. a): front view (heat shield), b): rear view on the lower side, s: separation line, a: attachment line, broken line(s): guessed pattern.

As explained above, attachment/reattachment lines lead to hot-spot situations, while separation lines lead to cold-spot situations. In case of the radiation-adiabatic wall this holds for the radiation-adiabatic temperature T_{ra} and for the heat flux in the gas at the wall q_{gw} . These two entities are directly related to each other, Chapter 9. In the following we consider therefore only the radiation-adiabatic temperature fields present on the lower side of the vehicle in the $M_\infty = 3$, $H = 35$ km case, Fig. 5.51 (left), and in the $M_\infty = 5$, $H = 41$ km case, Fig. 5.51 (right). Note that the figures are turned upside down, and that they have different color codes for the temperature.

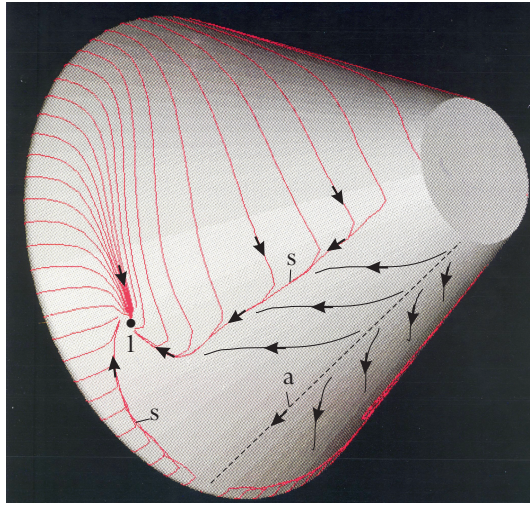


Fig. 5.50. Pattern of skin-friction lines on the surface of the VIKING 1 shape. $M_\infty = 5$, $H = 41$ km, $\alpha = -25^\circ$ [45]. Rear view on the lower side, s: separation line, a: attachment line, broken line(s): guessed pattern.

In the $M_\infty = 3$ case, the total temperature is around 660 K. Due to the surface radiation cooling we find (not shown), a radiation-adiabatic temperature of approximately 550 K at the stagnation point of the heat shield and at the upper shoulder, as well as at the heat-shield apex, where also a thinning of the boundary layer occurs. On the rear part, Fig. 5.51 (left), we get around point '1' (see Fig. 5.49) on the lower attachment line approximately 500 K, along the attachment line beginning in '3' approximately 400 K, which we find also on the upper side of the rear part of the vehicle. The lowest temperatures found are approximately 230–300 K in the region closer to the shoulder.

In the $M_\infty = 5$ case the total temperature is around 1,360 K. Due to the surface radiation cooling we find (again not shown), a radiation-adiabatic temperature of approximately 950 K at the stagnation point of the heat shield and at the upper shoulder, and a somewhat lower temperature at the heat-shield apex. On the rear part, Fig. 5.51 (right), we get on the lower attachment line initially approximately 600 K, and along the attachment line approximately 300 K. On the upper side of the rear part of the vehicle we have temperatures around 500 K. The lowest temperature is found with approximately 250 K at the location, where the vortex filament leaves the surface, point '1' in Fig. 5.50. This is as low as the lowest temperature in the $M_\infty = 3$ case.

Our results show that large surface-temperature differences can occur at the backsides of RV-NW's because also the backsides in general are radiation cooled. The temperature differences and hot-spot situations of course become more pronounced at higher flight Mach numbers. However, since the temperature of a radiation cooled surface depends also strongly on the (unit) Reynolds

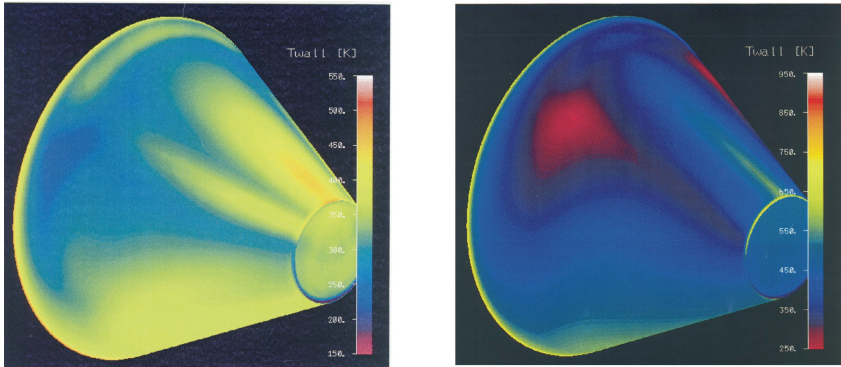


Fig. 5.51. Radiation-adiabatic wall temperature distribution, T_{ra} , on the rear part of the VIKING 1 shape for the free-stream conditions $M_\infty = 3$, $H = 35$ km, $\alpha = -25^\circ$ (left), and $M_\infty = 5$, $H = 41$ km, $\alpha = -25^\circ$ (right). The figures are turned upside down compared to the Figs. 5.48, 5.49 and 5.50 [45].

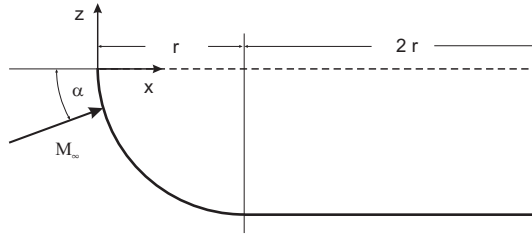
number [65], one always has to take into account flight speed and altitude, and also, of course, the attitude of the vehicle, in order to identify hot-spot and cold-spot situations. Their locations and temperature/heat-flux levels depend definitely on these parameters.

For the layout of the heat insulation of the backside of the vehicle thus the situation appears to be somewhat less clear-cut than for the layout of the frontal heat shield. Although at the backside of the vehicle the thermal loads are in general much smaller, also there the heat insulation must have a mass as low as possible.

All together we can say that a careful analysis of the entire flow field along the relevant parts of a flight trajectory (the re-entry trajectory) is necessary for getting a reliable data set regarding thermal loads. Flow-topology dependent hot-spot and cold-spot situations cannot be predicted with simple approximate methods. Coupled Euler/3-D boundary layer solutions in general will suffice on a windward side. On a leeward side with extensive flow separation/attachment and 3D vortical patterns, only solutions of the full Navier–Stokes equations permit to describe the actual situation accurately.

5.6 Problems

Problem 5.1 Given is a wedge-like body, which flies with an angle of attack α at M_∞ , Fig. 7.5. It has the length L , the width $w = 0.1L$, and a wedge angle θ . Assume Newtonian flow [65] and determine the location of the center-of-pressure as well as the necessary location of the center-of-gravity for longitudinal trim. Assume that the center-of-gravity lies on the axis ($z = 0$) of the body. The reference area is $A_{ref} = Lw = 0.1L^2$, and the reference length $L_{ref} = 0.5L$. Use the relations derived in Chapter 7.1.



Sketch of the generic contour of problem 5.4.

Problem 5.2 Consider the high Mach number flow past a double wedge (Figs. 7.5, 7.10), where the Newtonian approach is valid. Verify analytically that

- a) for a wedge angle $\phi_w = 45^\circ$ the configuration has no lift for an angle of attack $\alpha = 45^\circ$,
- b) for a wedge angle $\phi_w = 54,732^\circ$ the lift is negative for all angles of attack $\alpha > 0$.

Problem 5.3 The moments and in particular the components of the moments are dependent on the reference point. In the beginning of a design cycle and during the system development phase the center-of-gravity may be not well determined usually due to the open questions of the internal lay-out. Therefore the aerodynamicists define a fictitious moment reference point. At the end this requires a re-evaluation of the components of the moment if the center-of-gravity is ultimately defined.

Calculate the pitching moment of the Bicone_Tsnii shape for a reference location $x_{ref} = 0.42 L_{ref}$, $z_{ref} = -0.1467 L_{ref}$ for the flight point $M_\infty = 1.18$, $\alpha = 30^\circ$ by using the data of Fig. 5.24, where also the pitching moment for the reference point $x_{ref} = 0.57 L_{ref}$, $z_{ref} = -0.0667 L_{ref}$ is plotted. Compare with the data of Fig. 5.25. It is sufficient to extract approximately the data from Fig. 5.24. Use the relations derived in Chapter 7.1.

Problem 5.4 We consider a generic contour consisting of a quarter of a circle with radius r and a cylindrical part of length $2r$, see figure below. The angle of attack α moves between 0° and 90° .

Determine with the classical Newton method for hypersonic Mach numbers the relations for the aerodynamic coefficients C_X and C_Z and the coordinates of the center-of-pressure x_{cp} and z_{cp} as function of the angle of attack, first for the circle alone, and second for the complete contour. Use the three eqns. (7.5), (7.7), (7.9) and the information of Problems 5.1 and 5.2.

Evaluate for $\alpha = 0^\circ$ and $\alpha = 90^\circ$ these relations and justify them by drawing the results.

References

1. Smith, A.J.: Entry and Vehicle Design Considerations. Capsule Aerothermodynamics, AGARD-R-808, Paper 4 (1997)
2. Walberg, G.D.: A Survey of Aeroassisted Orbit Transfer. *J. of Spacecraft* 22(1), 3–18 (1985)
3. Charbonnier, J.M., Fraysse, H., Verant, J.L., Traineau, J.C., Pot, T., Masson, A.: Aerothermodynamics of the Mars Premier Orbiter in Aerocapture Configuration. In: *Proceedings 2nd Int. Symp. on Atmospheric Re-entry Vehicles and Systems*, Arcachon, France (2001)
4. Walberg, G.D., Siemers, P.M., Calloway, R.L., Jones, J.J.: The Aeroassist Flight Experiment. In: *IAF Conference*, Paper No. IAF-87-197, Brighton, England (1987)
5. Williams, L.J., Putnam, T.W., Morris, R.: Aeroassist Key to Returning from Space and the Case for AFE. Capsule Aerothermodynamics, AGARD-R-808, Paper 13 (1997)
6. Regan, F.J.: *Re-entry Vehicle Dynamics*. AIAA Education Series, New York, N.Y (1984)
7. Bertin, J.J.: *Hypersonic Aerothermodynamics*. AIAA Education Series, Washington, D.C. (1994)
8. Gupta, R.N., Moss, J.N., Price, J.M.: Assessment of Thermochemical Nonequilibrium and Slip Effects for Orbital Re-entry Experiment (OREX). AIAA-Paper 96-1859 (1996)
9. Paulat, J.C.: Atmospheric Re-entry Demonstrator Post Flight Analysis – Aerodynamics. In: *Proceedings 2nd Int. Symp. on Atmospheric Re-entry Vehicles and Systems*, Arcachon, France (2001)
10. Yamamoto, Y., Yoshioka, M.: CFD and FEM Coupling Analysis of OREX Aerothermodynamic Flight Data. AIAA-Paper 95-2087 (1995)
11. Murakami, K., Fujiwara, T.: A Hypersonic Flowfield Around a Re-entry Body Including Detailed Base Flow. ESA-SP-367 (1995)
12. Rumynski, A.N., Murzinov, I.N., Ivanov, N.M., Kazakov, M.N., Sobolevsky, V.G., Finchenko, V.S.: Comparative Multidisciplinary Analysis of Vehicles Intended for Descent on to the Earth Surface with the Mars Ground Samples. ESA-SP-487 (2002)
13. Way, D.W., Powell, R.W., Edquist, K.T., Masciarelli, J.P., Starr, B.R.: Aerocapture Simulation and Performance for the Titan Explorer Mission. AIAA-Paper 2003-4951 (2003)
14. Baillion, M., Pallegoix, J.F.: HUYGENS Probe Aerothermodynamics. AIAA-Paper 97-2476 (1997)
15. Baillion, M.: Aerothermodynamic Requirements and Design of the HUYGENS Probe. Capsule Aerothermodynamics, AGARD-R-808 (1997)
16. Burnell, S.I., Liever, P., Smith, A.J., Parnaby, G.: Prediction of the BEAGLE2 Static Aerodynamic Coefficients. In: *Proceedings 2nd Int. Symp. on Atmospheric Re-entry Vehicles and Systems*, Arcachon, France (2001)
17. Smith, A.J., Parnaby, G., Matthews, A.J., Jones, T.V.: Aerothermodynamic Environment of the BEAGLE2 Entry Capsule. ESA-SP-487 (2002)
18. Paulat, J.C., Baillion, M.: Atmospheric Re-entry Demonstrator Aerodynamics. In: *Proceedings 1st Int. Symp. on Atmospheric Re-entry Vehicles and Systems*, Arcachon, France (1999)

19. Moseley, W.C., Martino, J.C.: APOLLO Wind Tunnel Testing Programme – Historical Development of General Configurations. NASA TN D-3748 (1966)
20. Bertin, J.J.: The Effect of Protuberances, Cavities, and Angle of Attack on the Wind Tunnel Pressure and Heat Transfer Distribution for the APOLLO Command Module. NASA TM X-1243 (1966)
21. Blanchet, D., Kilian, J.M., Rives, J.: Crew Transport Vehicle-Phase B, Aerodynamic Data Base. CTV-Programme, HV-TN-8-10062-AS, Aerospatiale (1997)
22. Moseley, W.C., Moore, R.H., Hughes, J.E.: Stability Characteristics of the APOLLO Command Module. NASA TN D-3890 (1967)
23. Tran, P.: ARD Aerothermal Environment. In: Proceedings 1st Int. Symp. on Atmospheric Re-entry Vehicles and Systems, Arcachon, France (1999)
24. Ivanov, N.M.: Catalogue of Different Shapes for Unwinged Re-entry Vehicles. Final report, ESA Contract 10756/94/F/BM (1994)
25. Weiland, C.: Crew Transport Vehicle Phase A, Aerodynamics and Aerothermodynamics. CTV-Programme, HV-TN-3100-X05-DASA, Dasa, München/Ottobrunn, Germany (1995)
26. Marzano, A., Solazzo, M., Sansone, A., Capuano, A., Borriello, G.: Aerothermodynamic Development of the CARINA Re-entry Vehicle: CFD Analysis and Experimental Tests. ESA-SP-318 (1991)
27. Solazzo, M., Sansone, A., Gasbarri, P.: Aerodynamic Characterization of the CARINA Re-entry Module in the Low Supersonic Regimes. ESA-SP-367 (1995)
28. Lee, D.B., Bertin, J.J., Goodrich, W.D.: Heat Transfer Rate and Pressure Measurements Obtained During APOLLO Orbital Entries. NASA TN D-6028 (1970)
29. Lee, D.B., Goodrich, W.D.: The Aerothermodynamic Environment of the APOLLO Command Module During Superorbital Entry. NASA TN D-6792 (1972)
30. Bouslog, S.A., An, M.Y., Wang, K.C., Tam, L.T., Caram, J.M.: Two Layer Convective Heating Prediction Procedures and Sensitivities for Blunt Body Re-entry Vehicles. AIAA-Paper 93-2763 (1993)
31. Walpot, L.M.G.: Numerical Analysis of the ARD Capsule in S4 Wind Tunnel. ESA-SP-487 (2002)
32. Baillion, M., Tran, P., Caillaud, J.: Aerodynamics, Aerothermodynamics and Flight Qualities. ARCV Programme, ACRV-A-TN 1.2.3.-AS, Aerospatiale (1993)
33. Rochelle, W.C., Ting, P.C., Mueller, S.R., Colovin, J.E., Bouslog, S.A., Curry, D.M., Scott, C.D.: Aerobrake Heating Rate Sensitivity Study for the Aeroassist Flight Experiments. AIAA Paper, 89-1733 (1989)
34. Rousseau, S., Fraysse, H.: Study of the Mars Sample Return Orbiter Aerocapture Phase. In: Proceedings 2nd Int. Symp. on Atmospheric Re-entry Vehicles and Systems, Arcachon, France (2001)
35. Davies, C.B., Park, C.: Aerodynamics of Generalized Bent Biconics for Aero-Assisted, Orbital-Transfer Vehicles. *J. of Spacecraft* 22(2), 104–111 (1985)
36. Weiland, C., Haidinger, F.A.: Entwurf von Kapseln und deren aerothermodynamische Verifikation. In: Proceedings DGLR-Fachsymposium Strömungen mit Ablösung (not published) (November 1996)
37. Miller, C.G., Blackstock, T.A., Helms, V.T., Midden, R.E.: An Experimental Investigation of Control Surface Effectiveness and Real Gas Simulation for Biconics. AIAA-Paper 83-0213 (1983)
38. Park, C., Yoon, S.: Calculation of Real Gas Effects on Blunt Body Trim Angles. AIAA-Paper 89-0685 (1989)

39. Paulat, J.C.: Synthesis of Critical Points. MSTP-Programme, Final Report, HT-SF-WP1130-087-AS, Aerospatiale (1997)
40. N.N.: APOLLO Data Base. Industrial communication, Aerospatiale - Deutsche Aerospace Dasa (1993)
41. Moseley, W.C., Moore, R.H., Hughes, J.E.: Stability Characteristics of the APOLLO Command Module. NASA TN D-3890 (1967)
42. Yates, L.A., Venkatapathy, E.: Trim Angle Measurement in Free-Flight Facilities. AIAA-Paper 91-1632 (1991)
43. Wells, W.L.: Measured and Predicted Aerodynamic Coefficients and Shock Shapes for Aeroassist Flight Experiment Configurations. NASA TP-2956 (1990)
44. Dieudonne, W., Spel, M.: Entry Probe Stability Analysis for the Mars Pathfinder and the Mars Premier Orbiter. ESA-SP-544 (2004)
45. Hagmeijer, R., Weiland, C.: Crew Transport Vehicle Phase A, External Shape Definition and Aerodynamic Data Set. CTV-Programme, HV-TN-2100-011-DASA, Dasa, München/Ottobrunn, Germany (1995)
46. Weilmuenster, K.J., Hamilton II, H.H.: A Comparison of Computed and Experimental Surface Pressure and Heating on 70° Sphere Cones at Angles of Attack to 20°. AIAA-Paper 86-0567 (1986)
47. N.N.: CTV Aerodynamics. Industrial communication, Aerospatiale - Deutsche Aerospace Dasa (1995)
48. N.N.: CTV Dasa Data Base. Internal industrial communication, Dasa, München/Ottobrunn, Germany (1994)
49. Weiland, C., Pfitzner, M.: 3D and 2D Solutions of the Quasi-Conservative Euler Equations. Lecture Notes in Physics, vol. 264, pp. 654–659. Springer, Heidelberg (1986)
50. Pfitzner, M., Weiland, C.: 3D Euler Solutions for Hypersonic Free-Stream Mach Numbers. AGARD-CP-428, pp. 22-1–22-14 (1987)
51. Pallegoix, J.F., Collinet, J.: Atmospheric Re-entry Demonstrator Post Flight Analysis – Flight Rebuilding with CFD Control. In: Proc. 2nd Int. Symp. on Atmospheric Re-entry Vehicles and Systems, Arcachon, France (2001)
52. Paulat, J.C.: Synthesis of Critical Points. ESA Manned Space Transportation Programme, Final Report, HT-SF-WP1130-087-AS, Aerospatiale (1997)
53. Baillion, M.: Blunt Bodies Dynamic Derivatives. Capsule Aerothermodynamics, AGARD-R-808, Paper 8 (1997)
54. Chapman, G.T., Yates, L.A.: Dynamics of Planetary Probes: Design and Testing Issues. AIAA-Paper 98-0797 (1998)
55. Ericsson, L.E., Reding, J.P.: Re-Entry Capsule Dynamics. J. of Spacecraft 8(6), 579–586 (1971)
56. Whitlock, C.H., Siemers, P.M.: Parameters Influencing Dynamic Stability Characteristics of VIKING-Type Entry Configurations at Mach 1.76. J. of Spacecraft 9(7), 558–560 (1972)
57. Karatekin, Ö., Charbonnier, J.M., Wang, F.Y., Dehant, V.: Dynamic Stability of Atmospheric Entry Probes. ESA - SP - 544 (2004)
58. Wang, F.Y., Karatekin, Ö., Charbonnier, J.M.: Low-Speed Aerodynamics of a Planetary Entry Capsule. J. of Spacecraft 36(5), 659–667 (1999)
59. Teramoto, S., Fujii, K.: Study on the Mechanism of the Instability of a Re-entry Capsule at Transonic Speeds. AIAA-Paper 2000-2603 (2000)
60. Brockhaus, R.: Flugregelung. Springer, Heidelberg (2001)
61. Schueler, C.J., Ward, L.K., Hodapp, A.E.: Techniques for Measurement of Dynamic Stability Derivatives in Ground Test Facilities. AGARDograph 121 (1967)

62. Orlik-Rueckemann, K.J.: Techniques for Dynamic Stability Testing in Wind Tunnels. AGARD-RCP-235, Paper 1 (1978)
63. Giese, P., Heinrich, R., Radespiel, R.: Numerical Prediction of Dynamic Derivatives for Lifting Bodies with a Navier-Stokes Solver. Notes on Numerical Fluid Mechanics, vol. 72, pp. 186–193. Vieweg Verlag (1999)
64. Giese, P.: Numerical Prediction of First Order Dynamic Derivatives with Help of the Flower Code. Deutsches Zentrum für Luft- und Raumfahrt, TETRA Programme, TET-DLR-21-TN-3201 (2000)
65. Hirschel, E.H.: Basics of Aerothermodynamics. Progress in Astronautics and Aeronautics, AIAA, Reston, Va, vol. 204. Springer, Heidelberg (2004)
66. Tran, P., Soler, J.: Atmospheric Re-entry Demonstrator; Post Flight Analysis: Aerothermo Environment. In: Proceedings 2nd Int. Symp. on Atmospheric Re-entry Vehicles and Systems, Arcachon, France (2001)
67. Haidinger, F.A.: Numerical Investigation of the Heat Transfer on the Front Shield of a Capsule. Deutscher Luft- und Raumfahrtkongress, DGLR - JT96 - 0137 (1996)
68. Wilcox, D.C.: Turbulence Modelling for CFD. DCW Industries, La Cañada, CAL, USA (1998)
69. Hirschel, E.H.: Evaluation of Results of Boundary-Layer Calculations with Regard to Design Aerodynamics. AGARD R-741, pp. 5-1–5-29 (1986)